

1 **Embedding a One-column Ocean Model (SIT 1.06) in the**
2 **Community Atmosphere Model 5.3 (CAM5.3; CAM5–**
3 **SIT v1.0) to Improve Madden–Julian Oscillation**
4 **Simulation in Boreal Winter**

5

6 Yung-Yao Lan, Huang-Hsiung Hsu*, Wan-Ling Tseng, and Li-Chiang Jiang

7

8 Research Center for Environmental Changes, Academia Sinica, Taipei 11529, Taiwan

9 *Correspondence to: Huang-Hsiung Hsu (hhhsu@gate.sinica.edu.tw)

10 **Abstract**

11 The effect of the air–sea interaction on the Madden–Julian Oscillation (MJO)
12 was investigated using the one-column ocean model Snow–Ice–Thermocline (SIT
13 1.06) embedded in the Community Atmosphere Model 5.3 (CAM5.3; hereafter
14 CAM5–SIT v1.0). The SIT model with 41 vertical layers was developed to simulate
15 sea surface temperature (SST) and upper-ocean temperature variations with a high
16 vertical resolution that resolves the cool skin and diurnal warm layer and the upper
17 oceanic temperature gradient. A series of 30-year sensitivity experiments were
18 conducted in which various model configurations (e.g., coupled versus uncoupled,
19 vertical resolution and depth of the SIT model, coupling domains, and absence of the
20 diurnal cycle) were considered to evaluate the effect of air–sea coupling on MJO
21 simulation. Most of the CAM5–SIT experiments exhibit higher fidelity than the
22 CAM5-alone experiment in characterizing the basic features of the MJO such as
23 spatiotemporal variability and the eastward propagation in boreal winter. The overall
24 MJO simulation performance of CAM5–SIT benefits from (1) better resolving the
25 fine vertical structure of upper-ocean temperature and therefore the air–sea interaction
26 that result in more realistic intraseasonal variability in both SST and atmospheric
27 circulation and (2) the adequate thickness of a vertically-gridded ocean layer. The
28 sensitivity experiments demonstrate the necessity of coupling the tropical eastern
29 Pacific in addition to the tropical Indian Ocean and the tropical western Pacific.
30 Coupling is more essential in the south than north of the equator in the tropical
31 western Pacific. Enhanced MJO could be obtained without considering the diurnal
32 cycle in coupling.

Deleted: mixed layer.

Deleted: mixed

35 1. Introduction

36 The Madden–Julian Oscillation (MJO) is a tropical large-scale convection
37 circulation system that propagates eastward across the warm pool region from the
38 tropical Indian Ocean (IO) to the western Pacific (WP) on an intraseasonal time scale
39 (Madden and Julian, 1972). The MJO is not just an atmospheric phenomenon. The
40 findings from a multi-nation field campaign in the tropics called the Dynamics of
41 MJO/Cooperative Indian Ocean Experiment on Intraseasonal Variability in the Year
42 2011 (DYNAMO/CINDY2011; de Szoeke et al., 2017; Johnson and Ciesielski, 2017;
43 Pujiana et al., 2018; Yoneyama et al., 2013; Zhang and Yoneyama, 2017) revealed
44 vigorous air–sea coupling during the evolution of the MJO (Chang et al., 2019;
45 DeMott et al., 2015; Jiang et al., 2015, 2020; Kim et al., 2010; Li et al., 2016; Li et al.,
46 2020; Newman et al., 2009; Pei et al., 2018; Tseng et al., 2014). During the
47 suppression of convection, the MJO propagates eastward with light winds, which is
48 accompanied by enhanced downwelling shortwave radiation absorption, weaker
49 upward latent and sensible fluxes, less cloudiness and precipitation, and weaker
50 vertically turbulent mixing in the upper ocean, thus causing an increase in the upper-
51 ocean temperature. In the following active phase when deep convection occurs,
52 downwelling shortwave radiation is reduced and stronger westerly winds enhance
53 latent/sensible heat flux (LHF/SHF) loss from the ocean surface, thus causing a
54 decrease in the upper-ocean temperature (DeMott et al., 2015; Madden and Julian,
55 1972, 1994; Zhang, 2005).

56 In addition to the tropical ocean surface, the structure of the upper ocean also
57 evolves. Alappattu et al. (2017) reported that during an MJO event, surface flux
58 perturbations cause changes in the ocean thermohaline structure, thus affecting the
59 mixed-layer temperature. The following change in sea surface temperature (SST) can
60 further affect atmospheric circulation of the MJO. Variations in SST mediate LHF and

Deleted: vertical

62 SHF exchange across the air–sea interface. Although SST responds to atmospheric
63 forcing, the modulation of LHF and SHF provides feedback to the atmosphere
64 (DeMott et al., 2015; Jiang et al., 2020). Li et al. (2008, 2020) proposed that the phase
65 relationship between SST and convection implies a delayed air–sea interaction
66 mechanism whereby a preceding active-phase MJO may trigger an inactive-phase
67 MJO through the delayed effect of the induced SST anomaly over the IO. The
68 reduction in SST caused by a preceding active-phase MJO may, in turn, ~~yield~~ delayed
69 ocean feedback that initiates a suppressed-phase MJO, and vice versa. The by-no-
70 means negligible effect of intraseasonal SST variations caused by surface heat fluxes
71 suggests that the ocean state can affect the MJO (DeMott et al., 2015, 2019; Hong et
72 al., 2017; Li et al., 2020).

73 Since its discovery almost five decades ago, the MJO remains a phenomenon
74 that poses a challenge to the capacity of state-of-the-art atmospheric general
75 circulation models (AGCMs) such as those participating in the Coupled Model
76 Intercomparison Project phase 5 and 6 to generate successful simulations (Ahn et al.,
77 2017, 2020; Bui and Maloney 2018; Jiang et al., 2020; Hung et al., 2013; Kim et al.,
78 2011).

79 Recent studies have reported that air–sea coupling improves the representation of
80 the MJO in numerical simulation (Bernie et al., 2008; Crueger et al., 2013; DeMott et
81 al., 2015; Li et al., 2016; Li et al., 2020; Tseng et al., 2014; Woolnough et al., 2007).
82 Tseng et al. (2014) indicated that effectively resolving the ~~tropical~~ upper-ocean warm
83 layer to capture temperature variations in the upper few meters of the ocean could
84 improve MJO simulation. DeMott et al. (2015) suggested that the tropical
85 atmosphere–ocean interaction may sustain or amplify the pattern of the enhanced and
86 suppressed atmospheric convection of the eastward propagation. DeMott et al. (2019)
87 demonstrated that the improved MJO eastward propagation in four coupled models

Deleted: yields

89 resulted from enhanced low-level convective moistening for a rainfall rate of >5 mm
90 day⁻¹ due to air–sea coupling. In addition, numerical experiments have been
91 performed to investigate the effect of the diurnal cycle on the MJO (Hagos et al.,
92 2016; Oh et al., 2013), with the results suggesting that the strength and propagation of
93 the MJO through the Maritime Continent (MC) were enhanced when the diurnal cycle
94 was ignored.

95 Although previous studies have demonstrated the importance of considering the
96 air–sea interaction in a numerical model to improve MJO simulation, additional
97 details regarding model configuration (e.g., vertical resolution and total depth of the
98 vertically-gridded ocean, coupling domain, and absence of the diurnal cycle in air–sea
99 coupling) have not been systematically explored. Tseng et al. (2014) coupled the one-
100 column ocean model Snow–Ice–Thermocline (SIT; Tu and Tsuang, 2005) to the fifth
101 generation of the ECHAM AGCM (ECHAM5–SIT), in the tropics and indicated that a
102 vertical resolution of 1 m was essential to yield an improved simulation of the MJO
103 with a realistic strength and eastward propagation speed.

104 In this study, we coupled the SIT model to the Community Atmosphere Model
105 version 5.3 (CAM5.3; Neale et al., 2012)—the atmosphere component of the
106 Community Earth System Model version 1.2.2 (CESM1.2.2; Hurrell et al., 2013), —to
107 explore the improvement of MJO simulation by coupling SIT model to another
108 AGCM is reproducible in modeling science. The CAM5.3, which has been widely
109 used for the long-term simulation of the climate system, could not efficiently simulate
110 the eastward propagation of the MJO; instead, the model simulated a tendency for the
111 MJO to move westward in the IO (Boyle et al., 2015, Jiang et al, 2015). By contrast,
112 the updated CESM2 with the new CAM6 could realistically simulate the MJO (Ahn et
113 al., 2020; Danabasoglu et al., 2020). Thus, the well-explored CAM5, which does not
114 produce a realistic MJO, appears to be a favorable choice for exploring coupling a

Deleted: mixed layer

Deleted: -

Formatted: Pattern: Clear (White)

Deleted:)—

118 simple one-dimensional (1-D) ocean model over the tropical oceans, such as the SIT
119 model, can improve MJO simulation, as well as the effects of model configuration on
120 the degree of the improvement. Such a study can also enhance our understanding
121 regarding the effect of air–sea coupling on the MJO.

122 The MJO is a tropical atmosphere system that exhibits a more substantial
123 eastward propagation in boreal winter than in other seasons was the targeted feature in
124 this study. To examine the sensitivity of MJO simulations to different configurations
125 of the tropical air–sea coupling, we conducted a series of 30-year numerical
126 experiments by considering various model configurations (e.g., coupled versus
127 uncoupled, vertical resolution and depth of the SIT model, coupling domains, and
128 absence of the diurnal cycle) to investigate the effect of air–sea coupling. This paper
129 is organized as follows. Section 2 describes the data for validation, the model used for
130 simulation, and the design of numerical experiments. Section 3 describes the effect of
131 various tropical air–sea coupling configurations on the MJO simulation determined
132 through detailed MJO diagnostics. Discussion and conclusions are provided in
133 Section 4.

134

135 **2. Data, methodology, model description, and experimental designs**

136 **2.1 Data and methodology**

137 The data analyzed in this study include precipitation from the Global
138 Precipitation Climatology Project (GPCP), outgoing longwave radiation (OLR) and
139 daily SST (Optimum Interpolation SST; OISST) from the National Oceanic and
140 Atmosphere Administration (NOAA), and parameters from the ERA-Interim (ERA-I)
141 reanalysis (Adler et al., 2003; Dee et al., 2011; Lee et al., 2011; Reynolds and Smith,
142 1995; Schreck et al., 2018). The SST data for the SIT model were obtained from the
143 Hadley Centre Sea Ice and Sea Surface Temperature dataset (Rayner et al., 2003;

Formatted: Pattern: Clear (White)

Deleted: -

Deleted: -

146 HadISST1) and the ocean subsurface data (40-layer climatological ocean temperature,
147 salinity, and currents) for nudging were retrieved from the National Centers for
148 Environmental Prediction (NCEP) Global Ocean Data Assimilation System (GODAS;
149 Behringer and Xue, 2004).

150 We used the CLIVAR MJO Working Group diagnostics package (CLIVAR,
151 2009) and a 20–100-day filter (Kaylor, 1977; Wang et al., 2014) to determine
152 intraseasonal variability. MJO phases were defined following the index (namely,
153 RMM1 and RMM2) proposed by Wheeler and Hendon (2004), which ~~considered~~ the
154 first two principal components of the combined near-equatorial OLR and zonal winds
155 at 850 and 200 hPa. The band-passed filtered data were used for calculating the index
156 and defining phases.

Deleted: considers

157

158 **2.2 Model description**

159 **2.2.1 CAM5.3**

160 The CAM5.3 used in this study has a horizontal resolution of 1.9° latitude ×
161 2.5° longitude and 30 vertical levels with the model top at 0.1 hPa. The MJO could
162 not be realistically simulated in the CAM5.3. Boyle et al. (2015) demonstrated that
163 although making the deep convection dependent on SST improved the simulation of
164 the MJO variance, it exerted a significant negative effect on the mean-state climate of
165 low-level cloud and absorbed shortwave radiation. By comparing the simulation
166 results of an uncoupled and coupled CAM5.3, Li et al. (2016) suggested that air–sea
167 coupling and the convection scheme most significantly affected the MJO simulation
168 in the climate model.

169

170 **2.2.2 1-D high-resolution TKE ocean model**

171 The 1-D high-resolution turbulence kinetic energy (TKE) ocean model SIT was

173 used to simulate the diurnal fluctuation of SST and surface energy fluxes (Lan et al.,
174 2010; Tseng et al., 2014; Tu and Tsuang, 2005). [A description of the 1-D high-](#)
175 [resolution ocean model SIT can be found in the appendix.](#) The model was well
176 verified against in situ measurements on board the R/V Oceanographic Research
177 Vessel 1 and 3 over the South China Sea (Lan et al., 2010) and on R/V Vickers over
178 the tropical WP (Tu and Tsuang, 2005).

179 The SIT model determines the vertical profiles of the temperature and
180 momentum of a water column from the surface down to the seabed, except in the
181 fixed ocean model bottom experiment. The default setting of vertical discretization
182 (e.g., in the control coupled experiment) is 41 layers with 12 layers in the first 10.5 m,
183 6 layers between 10.5 m and 107.8 m ([appendix Fig. A1](#)). In the 1-D TKE ocean
184 model, temperature and salinity below 107.8 m, where vertical turbulent mixing is
185 greatly weakened, are nudged toward the climatological values of GODAS data until
186 4607 m. The extra high vertical resolution is needed to catch detailed temporal
187 variation of upper ocean temperature characterized by the warm layer and cool skin
188 (Tu and Tsuang, 2005). To account for the neglected horizontal advection heat flux,
189 the ocean is weakly nudged (by using a 30-day time scale) between 10.5 m and 107.8
190 m and strongly nudged (by using a 1-day time scale) below 107.8 m according to the
191 NCEP GODAS climatological ocean temperature. No nudging is performed within
192 the upper-most 10.5 m. The SIT model calculates twice for each CAM5 time step (30
193 min; i.e., coupling 48 times per day).

194

195 **2.3 Experimental design**

196 A series of 30-year numerical experiments (Table 1) were conducted to
197 investigate the effect of the air–sea interaction on the MJO simulation. The HadSST1
198 used to force the coupled and uncoupled model was the climatological monthly-mean

Deleted: Supplementary Information I).

200 SST averaged over 1982-2001. The monthly SST was linearly interpolated to daily
201 SST fluctuation that forced the model. The SST in the air-sea coupling tropical
202 region was recalculated by the SIT during the simulation, while the prescribed annual
203 cycle of SST was used in the areas outside the coupling region. Ocean bathymetry of
204 the SIT was derived from the NOAA ETOPO1 data (Amante and Eakins, 2009) and
205 interpolated into $1.9^{\circ} \times 2.5^{\circ}$ horizontal resolution.

206 All simulations were driven by the prescribed annual cycle of SST repeatedly for
207 30 years. The strategy is to evaluate the simulation capacity of climate models under
208 the same condition without considering interannual variation induced by SST. This
209 approach has been widely adopted in many studies (Delworth et al., 2006; Haertel et
210 al., 2020; Subramanian et al., 2011; Tseng et al., 2014; Wang et al., 2005).

211 Atmospheric initial conditions and external forcing such as CO₂, ozone, and
212 aerosol in near-equilibrium climate state around the year 2000 were taken from
213 F_2000_CAM5 component set based on CESM1.2.2 framework development. The
214 data has been commonly used in present-day simulations using CAM5 (e.g., He et al.,
215 2017).

216 The setup of five sets of experiment conducted in this study are described as
217 follows.

218 (1) A standalone CAM5.3 simulation forced by climatological monthly HadISST1
219 (A-CTL) and the control experiment of coupled CAM5-SIT simulation (C-
220 30NS; 41 vertical levels, coupling in the entire tropics between 30°N and 30°S
221 with a diurnal cycle). The reasons for tropical coupling are two folds.
222 Considering that the MJO is essentially a tropical phenomenon, the coupling was
223 implemented only between 30°N and 30°S. Secondly, coupling a one-
224 dimensional ocean model in the extratropics without surface flux correction as in

225 our case would ignore the impacts of strong ocean currents (such as the Kuroshio
226 and Gulf Stream) and result in large biases.

227 (2) Upper-ocean vertical resolution experiment: Two simulations with the first layer
228 centering at 12 m (C-LR12m) and 34 m (C-LR34m). Further details of the
229 experimental design are shown in appendix Fig. A1. This experiment is to
230 demonstrate the significant improvement that a fine vertical resolution can
231 achieve compared to the coarse resolution (e.g., tens of meters) that is often
232 adopted in slab ocean model.

Deleted: supplementary Fig. S1

Formatted: Font color: Auto

233 (3) Shallow ocean bottom experiment: Three simulations with the ocean model
234 bottom at 10 m (C-HR1mB10m), 30 m (C-HR1mB30m), and 60 m (C-
235 HR1mB60m) (appendix Fig. A2). Note that all experiments retained the same
236 vertical resolution (e.g., 1 meter in the first top 10 meters of the ocean) but with
237 various ocean bottom (i.e., 10, 30, and 60 meters). The purpose is to demonstrate
238 how the total ocean heat content, which depends on the total depth of the ocean,
239 can affect the MJO.

Deleted: supplementary Fig. S2).

240 (4) Regional coupling experiment: Four simulations with the coupling region in 0°N-
241 30°N (C-0_30N) and 0°S-30°S (C-0_30S) for latitudinal effect, and 30°E-
242 180°E (C-30_180E) and 30°E-75°W (C-30E_75W) for longitudinal effect. The
243 coupling domains are shown in Fig. 1. In this experiment we identified the key
244 ocean basins where coupling is essential.

245 (5) Diurnal cycle experiment: To explore the effect of diurnal coupling cycle a non-
246 diurnal simulation was conducted for a comparison with the C-30NS simulation.
247 The non-diurnal simulation (C-30NS-nD), considers the air-sea interaction only
248 once a day, namely, calculating SHF and LHF based on daily mean atmospheric
249 variables and SST. To prevent the inconsistent local time in different regions, the
250 coupling frequency at each grid point remained 48 times per day using the same

Deleted: A

Deleted: that

255 daily means of atmospheric variables and SST at that particular point. In
256 contrast, the control simulation calculates air-sea fluxes 48 times a day based on
257 instantons values. A comparison between the non-diurnal simulation and the
258 control simulation reveals the effect of diurnal cycle in air-sea coupling.

Deleted: -

Deleted: air0sea

259

260 3. Results and Discussion

261 The realistic simulation of the MJO has always been a major bottleneck in the
262 development of climate models. In this section, we demonstrate the sensitivity of air-
263 sea coupling experiments using a 1-D high-resolution ocean model significantly
264 improves the MJO simulation by the CAM5.3. The period between November and
265 April when the MJO is the most prominent was the targeted season in this study.

266

267 3.1 Improvement of MJO simulation through air-sea coupling

268 This subsection compares the MJO simulation of the control coupled
269 experiment (C-30NS) with that of the uncoupled AGCM (A-CTL) forced by
270 climatological monthly SST of HadISST1 to demonstrate the effect of air-sea
271 coupling on the MJO simulation by coupling the SIT model to the CAM5.3 in the
272 tropical belt (30°N-30°S).

273

274 3.1.1 Wavenumber-frequency spectra and eastward propagation characteristics

275 A wavenumber-frequency spectrum (W-FS) analysis was conducted to quantify
276 propagation characteristics simulated in different experiments. The spectra
277 of unfiltered U850 in ERA-I reanalysis, C-30NS, and A-CTL are shown in Fig. 2a-c,
278 respectively. The C-30NS considering the coupling in 30°N-30°S realistically
279 simulates eastward-propagating signals at zonal wavenumber 1 and 30-80-day
280 periods (Fig. 2a-b), although with a slightly larger amplitude compared with ERA-I.

283 By contrast, the uncoupled A–CTL does not yield realistic simulation; instead, it
284 simulates both eastward (wavenumber 1)- and westward (wavenumber 2)-propagating
285 signals with an unrealistic spectral shift to time scales longer than 30–80-day.

286 The major features of the simulated MJO propagation were examined. Figure
287 2d–f show the time evolution of precipitation and U850 anomalies in Hovmöller
288 diagrams, which represent lagged correlation coefficients between the precipitation
289 averaged over 10°S–5°N, 75–100°E and the precipitation and U850 averaged over
290 10°N–10°S on intraseasonal timescales. Figure 2d indicates eastward propagation for
291 both precipitation and U850 from the eastern IO to the dateline, with precipitation
292 leading U850 by approximately a quarter of a cycle. The Hovmöller diagram derived
293 from the C–30NS (Fig. 2e) exhibits the key characteristics of eastward propagation
294 for both precipitation and U850 and the relative phases between the two, although the
295 simulated correlation is slightly weaker than that derived from GPCP and ERA-I. By
296 contrast, the uncoupled A–CTL simulates intraseasonal signals that propagate
297 westward over the IO and weak and much slower eastward propagation crossing the
298 MC and WP (Fig. 2f). The contrast between Fig. 2e and 2f demonstrate that coupling
299 a 1-D TKE ocean model alone could lead to a significant improvement in an AGCM
300 in simulating the major characteristics (e.g., amplitude, propagation direction and
301 speed, and phase relationship between precipitation and circulation) of the MJO.

302

303 **3.1.2 Coherence of the simulated MJO**

304 Cross-spectral analysis was conducted to examine the coherence and phase lag
305 between tropical circulation and convection, which were plotted over the tropical
306 wave spectra. Figure 2g–i show the symmetric part (e.g., Wheeler and Kiladis, 1999)
307 of OLR and U850 in ERA-I/NOAA data, C–30NS, and A–CTL, respectively. We
308 present only the spectra between 0 to 0.35 day⁻¹ to highlight the MJO and equatorial

309 Kelvin waves. The most prominent characteristics seen in ERA-I/NOAA data are the
310 peak coherence at wavenumbers 1–3 and a phase lag of approximately 90° in the 30–
311 80-day band (Ren et al., 2019; Wheeler and Kiladis 1999). The coupled experiment
312 C–30NS simulates strong coherence in this low-frequency band (wavenumber 1) and
313 exhibits a realistic phase lag relationship between U850 and OLR perturbations.
314 However, the coherence at wavenumbers 2–3 for the 30–80-day period simulated by
315 C–30NS is weaker than that in ERA-I/NOAA data. This undersimulation was also
316 noted in CCSM4 (Subramanian et al., 2011), the uncoupled and coupled CAM4 and
317 CAM5 (Li et al., 2016), and NorESM1-M (Bentsen et al., 2013), which had a version
318 of the CAM as an AGCM. In summary, C–30NS considering the coupling between
319 30°N – 30°S produces coherent and energetic patterns in the eastward-propagating
320 intraseasonal fluctuations of U850 and OLR in the tropical IO and WP that are
321 generally consistent with the MJO characteristics. By contrast, the MJO
322 characteristics in A–CTL are considerably weaker than those in C–30NS and that in
323 ERA-I/NOAA data.

324

325 **3.1.3 Horizontal and vertical structures of the MJO across the MC**

326 Figure 2j–o show the horizontal and vertical structures of the MJO when deep
327 convection is the strongest over the MC (i.e., phase 5). Figure 2j–l present the 20–
328 100-day filtered OLR (W m^{-2} , shaded) and 850-hPa wind (m s^{-1} , vector). C–30NS
329 realistically simulated the enhanced tropical convection over the eastern IO and the
330 Kelvin-wave-like easterly anomalies over the tropical WP despite undersimulating
331 the convection over the MC (Fig. 2j and 2k). By contrast, A–CTL failed to simulate
332 the enhanced convection over the eastern IO and MC; instead, it simulated
333 considerably weaker convection and easterly winds over the MC and WP,
334 respectively, than that in ERA-I/NOAA data (Fig. 2j and 2l).

335 Figure 2m–o show the vertical–longitudinal profiles of 20–100-day filtered
336 15°N–15°S averaged vertical velocity (OMEGA; Pa s⁻¹, shaded) and moist static
337 energy tendency (dMSE/dt) anomalies (W m⁻², contour) at phase 5. The spatial
338 distribution of negative OMEGA (ascending motion) anomalies generally agreed with
339 OLR anomalies in C–30NS simulation and NOAA data over the Indo-Pacific region
340 (Fig. 2m and 2n). The relatively spatial relationship between the ascending motion
341 and dMSE/dt seen in ERA-I is well simulated in the coupled experiment C–30NS. For
342 example, positive dMSE/dt anomalies on the eastern side of the anomalous ascent
343 demonstrate that the energy recharge process occurs in advance of the MJO
344 convection over the lower-tropospheric easterlies (Fig. 2m and 2n), whereas negative
345 dMSE/dt anomalies on the western side reveal that the discharge process occurs
346 during and after convection over the lower-tropospheric westerlies. By contrast, this
347 phase relationship, considered to be an essential feature leading to the eastward
348 propagation of an MJO (Hannah and Maloney 2014; Heath et al., 2021), is not
349 properly simulated in the uncoupled experiment A–CTL (Fig. 2o), in which the
350 simulated weak negative OMEGA is located between negative and positive dMSE/dt
351 anomalies over weak lower-tropospheric wind anomalies and associated with weak
352 convection over the MC (Fig. 2l).

Deleted: (MSE

Deleted: MSE

Deleted: MSE

Deleted: MSE

Deleted: MSE

353 The temporal evolution of NOAA OLR and ERA-I U850 (Fig. 3a) indicates
354 that convection originating in the western IO is enhanced during its eastward
355 propagation to the MC where it reaches the peak amplitude and then gradually
356 weakened when continuing moving eastward to the dateline. In the coupled
357 experiment C–30NS, this evolution of convectively coupled circulation is realistically
358 simulated, although it is weaker than the strength seen in NOAA OLR (Fig. 3b).
359 Moreover, the split of convection into two cells off the equator in phase 6 is
360 appropriately simulated in C–30NS (P6 in Fig. 3a and 3b). This split was caused by

366 the topographic and land–sea contrast effects of the MC (Tseng et al., 2017).
367 Associated with the split is the southward detouring of the anomalous convection
368 during the passage of the MJO through the MC (Kim et al. 2017, Tseng et al., 2017;
369 Wu and Hsu, 2009). After the passage of the MJO through the MC, the anomalous
370 convection stays south of the equator and continues moving eastward to the
371 dateline. In the uncoupled A–CTL, the systematic eastward propagation of
372 convectively coupled MJO circulation from the IO into the MC is not simulated.
373 Instead, the convection over the MC develops in situ at a later stage than that
374 observed (e.g., P6 in Fig. 3c) and dissipated rapidly. The A–CTL simulates a pair of
375 off-equator convection anomalies in the eastern IO during phase 2 (P2 in Fig. 3c) that
376 moves westward toward the central IO and were amplified at later stages (e.g., P4 in
377 Fig. 3c). This unrealistic evolution explains the westward propagation tendency
378 observed in the Hovmöller diagram (Fig. 2f).

379

380 **3.1.4 Characteristics of air–sea interaction**

381 Figure 4a–c show the longitude–phase diagram in which the 20–100-day filtered
382 precipitation (shaded) and SST (contour) anomalies were averaged over 10°S–10°N to
383 determine the relationship between precipitation and SST fluctuations and to establish
384 a link between air–sea coupling and convection. The propagation of the enhanced
385 convection with positive SST anomalies to the east could be clearly seen in
386 GPCP/OISST and the coupled experiment C–30NS (Fig. 4a and 4b). The highest SST
387 anomaly (SSTA) leads the maximum precipitation anomaly by approximately 2–3
388 phases, and the SSTA begins to decrease following the onset of enhanced
389 precipitation. The ERA-I and OISST data reveal the following relationship between
390 net surface flux and SST: the decreased (increased) LHF/SHF and increased
391 (decreased) downward radiation flux leading (lagging) the positive (negative) SSTA

392 east (west) of anomalous deep convection. This well-known lead–lag relationship
393 reflecting the active air–sea interaction in an MJO is realistically simulated in the
394 coupled experiment C–30NS (not shown).

395 The contrast between C–30NS and A–CTL confirms the key role of the air–sea
396 interaction in contributing to the eastward propagation and demonstrates that the
397 eastward propagation simulation can be markedly improved by incorporating the air–
398 sea interaction process in the model, even when using a simple 1-D ocean model such
399 as SIT.

400

401 **3.1.5 Vertically tilting structure**

402 The warm SST was the key forcing that contributed to the boundary layer
403 convergence before the onset of deep convection (Li et al., 2020; Tseng et al., 2014).
404 Hence, the warmer upper ocean enhances the low-level atmospheric convergence and
405 then leads to enhanced low-level moisture and preconditioned deep convection and
406 eastward propagation. This moistening process associated with warm ocean surface
407 temperature is well simulated in the coupled experiment C–30NS but is not shown
408 here. Instead, we present the coupling of moisture divergence (MD) and atmospheric
409 circulation.

410 MD and zonal wind anomalies from the surface to the upper troposphere
411 averaged over the 10°S–10°N and 120–150°E region are shown in Fig. 4d–f to depict
412 the relationship between the vertically tilting structure of MD and zonal wind
413 anomalies. Note that the active convection occurred around phase 5. The coupled
414 experiment C–30NS (Fig. 4e) realistically simulates the deepening of coupled MD
415 and zonal wind anomalies with time (Fig. 4d). An evolution from the right to left
416 seen in each panel of Fig. 4d–f is equivalent to the eastward movement of vertically
417 tilting circulation from the eastern IO into the MC because of the eastward-

418 propagating nature of the MJO. Figure 4d and 4e show that in both ERA-I reanalysis
419 and the coupled experiment C-30NS, the near-surface convergence (negative MD)
420 occurring in the easterly anomalies lead the convection and continued deepening up
421 to 500 hPa from phase 2 to phase 6 when the easterly anomalies switch to westerly
422 anomalies. By contrast, this evolution of coupled MD-zonal wind anomalies are not
423 appropriately simulated in the uncoupled experiment (Fig. 4f). For example, a slow
424 deepening with time is observed in the MD anomaly but not in the zonal wind
425 anomaly that exhibits a vertically decayed structure, suggesting that MD and wind
426 anomalies are not well coupled, as noted in the ERA-I/NOAA data and the control
427 coupled experiment.

428 In the ERA-I reanalysis data, the negative near-surface MD anomalies appear
429 first under the easterly anomaly and continue deepening between the easterly and
430 westerly anomalies. This development in the phase relationship between MD and
431 zonal wind anomalies in both ERA-I reanalysis data and the coupled simulation is
432 consistent with the well-known structure embedded in the MJO, namely the near-
433 surface convergence in the easterly phase (i.e., a boundary-layer moistening process;
434 Kiranmayi and Maloney 2011; Li et al., 2020; Tseng et al., 2014), followed by the
435 deep convection when transitioning to the westerly phase. This close phase
436 relationship that is key to the eastward propagation is appropriately simulated in the
437 coupled experiment but not in the uncoupled experiment.

438

439 **3.1.6 Intraseasonal variance of precipitation**

440 Figure 4g-i present the spatial distribution of intraseasonal variance of
441 precipitation. In the GPCP data, the maximum variance is noted over the tropical
442 eastern IO, MC, and tropical WP. The maximum variance south of the island in the
443 MC and the equator in the tropical WP reflects the southward shift of the MJO deep

444 convection when passing through the MC, partly due to the blocking effect of
445 mountainous islands and the higher moisture content over high SST south of the
446 equator in the region during boreal winter (Kim et al., 2017; Ling et al., 2019; Sobel
447 et al., 2008; Tseng et al., 2017; Wu and Hsu, 2009). Although the control coupled
448 experiment fails to simulate the variance maximum in the tropical eastern IO, it
449 appropriately simulates the maximum variance over the tropical WP, reflecting its
450 ability to simulate the eastward propagation of the MJO through the MC. By contrast,
451 the uncoupled A-CTL experiment simulates considerably weaker intraseasonal
452 variance in both the tropical eastern IO and the tropical WP. Figure 4j-l are the 20-
453 100-day filtered SST (K, shaded) and 850-hPa wind (m s^{-1} , vector) during MJO
454 phase 7 when deep convection is the strongest over the dateline. The coupled
455 experiment C-30NS realistically simulates the negative SST anomaly over the MC
456 and WP when enhanced tropical convection passed through the MC to the dateline,
457 indicating the capability of the SIT model to reproduce the SST anomaly by
458 exchanging LHF/SHF between the atmosphere and ocean. In A-CTL, no SST
459 anomaly is evident because the model was forced by prescribed climatological SST.
460 The contrast seen in Fig. 4j-l demonstrates the essential role of atmosphere-ocean
461 coupling in shaping the MJO. A delayed air-sea interaction mechanism was noted,
462 where a preceding active-phase MJO may trigger an inactive-phase MJO through the
463 delayed effect of the induced SST anomaly. In addition, the westerly winds at 850
464 hPa moving southward between MC and WP are captured by the control experiment
465 C-30NS and are similar to the ERA-I reanalysis winds (Fig. 4j and 4k). By contrast,
466 A-CTL forced by climatological monthly SST ($<0.05 \text{ K phase}^{-1}$ anomaly) fails to
467 simulate the southward westerly wind of the region extending from the MC to the
468 dateline (Fig. 4l).

469

470 **3.2 Effect of upper-ocean vertical resolution**

471 In the control coupled experiment C-30NS, the vertical resolution in the upper
472 10.5 m was 1 m. Tseng et al. (2014) suggested that fine vertical resolution is crucial
473 for appropriately simulating the eastward propagation. To investigate the effect of
474 vertical resolution, two experiments with a thicker first layer were conducted by
475 moving the center of the layer to 11.5 m (C-LR12m) and 33.9 m (C-LR34m),
476 respectively, as opposed to the control experiment in which 10 layers were
477 implemented in the first 10.5 meters (see [appendix Fig. A1 for vertical discretization](#)).

Deleted: supplementary Fig. S1 for vertical discretization).

478 The dramatic changes in vertical profile of ocean temperature between the fine and
479 coarse resolution simulation are demonstrated in Fig.5, which presents the 20–100-
480 day filtered oceanic temperature anomalies (K, shaded) between 0 and 60 m depth for
481 MJO phase 1, 3, 5, and 7. The amplitude of ocean temperature is the largest in C-
482 30NS and much weaker in C-LR12m and C-LR34m. In addition, there is a clear
483 vertical stratification of ocean temperature in C-30NS, whereas C-LR12m and C-
484 LR34m are well mixed because of not vertically gridded. This demonstrates the
485 necessity of fine vertical gridding for resolving the quick fluctuation of ocean
486 temperature when interacting with the atmosphere.

487 The W-FS spectral peaks of U850 in C-LR12m are concentrated in eastward-
488 propagating wavenumber 1 at three timescales (e.g., longer than 80 days, 30–80 days,
489 and approximately 30 days; Fig. [6a](#)). In C-LR34m, both eastward and westward
490 signals are simulated with the dominant W-FS timescale longer than 80 days (Fig.
491 [6b](#)). The appearance of both eastward and westward signals at a lower frequency
492 implied a stronger stationary tendency or weaker eastward-propagating tendency. This
493 result is consistent with that reported by Tseng et al. (2014) that the scientific
494 reproducibility of coarser resolution causes a longer intraseasonal periodicity and
495 slower eastward propagation of the MJO.

Deleted: 5a

Deleted: 5b

499 The effect of vertical resolution on the MJO simulation can be seen in the
 500 Hovmöller diagram. The eastward propagation simulated in C–LR12m (Fig. 6c)
 501 markedly weakened after crossing the MC compare with that simulated in the control
 502 experiment C–30NS (Fig. 2e). In C–LR34m, the quasi-stationary fluctuation and
 503 westward propagation are simulated over the IO (Fig. 6d), appearing similar to those
 504 in A–CTL (Fig. 2f). The lead–lag relationship between precipitation (zonal wind) and
 505 SST is poorly simulated in C–LR12m (Fig. 6e) and even more poorly simulated in C–
 506 LR34m (Fig. 6f). This result confirms the finding reported by Tseng et al. (2014) that
 507 a higher vertical resolution in the upper few meters below the surface allows for a
 508 faster air–sea interaction, thus resulting in a more realistic simulation of the MJO.

Deleted: 5c

Deleted: 5d

Deleted: 5e

Deleted: 5f

510 3.3 Effect of the lowest boundary of the SIT model

511 The ocean is a vital energy source for the MJO. Although vertical resolution is
 512 crucial for the efficiency of air–sea interaction, the thickness of the upper ocean that
 513 interacts with the atmosphere represents the ocean heat content to substantiate the
 514 MJO. A key question is how the total ocean heat content, which depends on the total
 515 depth of the ocean, can affect the MJO. Considering two models with the same
 516 vertical resolution, the model with thinner ocean (e.g., 10 meter) would interact as
 517 efficiently as another model with thicker ocean (e.g., 60m) but with much less heat to
 518 release to or to absorb from the atmosphere. The former would have less impact on
 519 the atmosphere than the latter. Using the same vertical resolution, three experiments
 520 with various ocean depths ocean, bottom at 10, 30, and 60 m, were conducted (see
 521 appendix Fig. A2 and Table 1).

Deleted: mixed layer should be for a realistic simulation. To explore this issue, three experiments with a model ocean with a 1-m

Formatted: Font color: Auto, Pattern: Clear (White)

Deleted: thick a vertically-gridded

Formatted: Font color: Auto, Pattern: Clear (White)

Formatted: Font color: Auto, Pattern: Clear (White)

Deleted: and

Formatted: Font color: Auto, Pattern: Clear (White)

Formatted: Font color: Auto, Pattern: Clear (White)

Formatted: Font color: Auto, Pattern: Clear (White)

Deleted: (SIT)

Deleted: , which included the top 12, 14, and 16 levels, respectively, as shown in supplementary Fig. S2 and Table 1,

Formatted: Font color: Auto, Pattern: Clear (White)

Deleted: .

Formatted: Font color: Auto, Pattern: Clear (White)

Deleted: 6a

Deleted: 6d

522 The spectra and the Hovmöller diagrams shown in Fig. 7a–c and Fig. 7d–f,
 523 respectively, demonstrate that the thicker ocean model simulates a stronger MJO with
 524 a frequency closer to those in the coupled experiment C–30NS and ERA-I/NOAA

540 data, and more realistic eastward propagation. In addition, the lead–lag relationship
541 between precipitation (wind) and SST is more realistically simulated with increasing
542 thickness of the ocean model (Fig. 7g–i).

Deleted: 6g

543 This result suggests that the thickness of the vertically-gridded ocean that interacts
544 with the atmosphere strongly affects the frequency of the simulated MJO. A thinner
545 (thicker) vertically-gridded ocean is more quickly (slowly) recharged and discharged

Deleted: oceanic mixed layer

546 through SHF and LHF exchange between the atmosphere and ocean and therefore
547 likely fluctuates at a faster (slower) tempo. The simulated periodicity is therefore
548 affected by the thickness (or ocean heat content) of upper ocean that interacts

Deleted: oceanic mixed layer

549 rigorously with the atmosphere. Although the result suggests 60 m is an appropriate

Formatted: Font color: Auto, Pattern: Clear (White)

Deleted: of oceanic mixed layer

Deleted: .)

550 thickness to realistically simulate the periodicity of the MJO, we did not intend to
551 suggest the exact thickness required for a proper simulation because it might depend
552 on the model. The upper ocean should be adequately thick to contain a certain amount

Deleted: oceanic mixed layer

553 of heat to generate appropriate periodicity. However, the reason for the intraseasonal
554 time scale (i.e., 20-100 days) should be determined in future studies. This finding
555 does not suggest a constant periodicity because periodicity might be affected by the
556 time-varying structure of the atmosphere and ocean in the real world.

557

558 3.4 Effects of coupling domains

559 The MJO is a planetary-scale phenomenon. Given its large-scale circulation, the
560 air–sea interaction affecting the MJO likely occurs in a much larger area than the
561 region near the major convection anomalies. In this section, we discuss the effect of
562 coupling domain on model ability to simulate the eastward propagation speed and
563 periodicity of the MJO. Four experiments considering the coupling in various
564 domains (C–0_30N, C–0_30S, C–30_180E, and C–30E_75W, Fig. 1) were conducted
565 for the purpose. The results are shown in Fig. 8. The C–0_30N that considered the

Deleted: 7

573 coupling in the tropics between the equator and 30°N simulates the least realistic MJO
574 propagation in terms of W–FS (Fig. 8a), zonal wind–precipitation coupling (Fig. 8e),
575 and SST–precipitation (Fig. 8i) among the four regional coupling experiments. By
576 contrast, coupling only the tropics between the equator and 30°S simulates a more
577 realistic MJO in all three aspects (i.e., spectrum in Fig. 8b, temporal evolution of
578 precipitation/wind, and precipitation/SST coupling in Fig. 8f and 8j). Figure. 9a
579 indicates that the negative OLR anomalies at phase 5 simulated in C–0_30N stays
580 mainly north of the equator and does not shift southward in the MC as revealed in
581 ERA-I reanalysis and NOAA OLR and in the control experiment C–30NS, and the
582 convection over the IO is unrealistically weak. By contrast, the southward detouring
583 in the MC is realistically simulated in C–0_30S that coupled only the tropical ocean
584 between the equator and 30°S. This result indicates that air–sea coupling occurring
585 south of the equator is the key to producing appropriate eastward propagation and
586 detouring of the MJO through the MC. Without this coupling, the C–0_30N
587 experiment fails to realistically simulate the eastward propagation of the MJO (Fig.
588 8e). This contrast can be attributed to the warmer ocean surface and higher moisture
589 content found south of the equator in boreal winter, which comprise a more favorable
590 environmental condition for air–sea coupling and convection–circulation coupling and
591 the occurrence of the MJO.

592 MJO simulations can be affected by air–sea coupling in the longitudinal domain.
593 Tseng et al. (2014) examined this effect by allowing coupling in different regions
594 (e.g., the IO, WP, and IO + WP) and found that the IO + WP coupling experiment
595 yielded the most satisfactory MJO simulation in terms of the zonal W–FS and
596 eastward propagation characteristics. In this study, we conducted sensitivity
597 experiments in which we allowed coupling in the tropics in two longitudinal domains,
598 namely 30°E–180°E (C–30_180E) and 30°E–75°W (C–30E_75W). The 30°E–180°E

Deleted: 7a

Deleted: 7c

Deleted: 7i

Deleted: 7b

Deleted: 7f

Deleted: 7j

Deleted: 8a

Deleted: 7e

607 region covered the IO and WP, and the 30°E–75°W region covered the IO and the
608 entire tropical Pacific. As shown in Fig. 8, the C–30E_75W experiment simulates
609 more realistic MJO than the C–30_180E experiment, with stronger eastward
610 propagation and larger amplitudes in the spectrum (Fig. 8c and 8d) and Hovmöller
611 diagrams of precipitation/wind (Fig. 8g and 8h) and precipitation/SST (Fig. 8k and
612 8l). The simulated MJO in C–30E_75W propagated farther east than that in C–
613 30_180E, particularly evident in Fig. 8k and 8l. The spatial distributions of circulation
614 and OLR shown in Fig. 9c and 9d indicate the presence of a stronger convective-
615 coupled circulation system over the MC and WP in C–30E_75W. These results
616 suggest that coupling over the entire tropical IO and Pacific could enhance the
617 strength and eastward propagation of the MJO and encourage farther propagation to
618 the central Pacific.

619

620 3.5 Diurnal versus no diurnal cycle in air–sea coupling

621 Previous studies showed that the diurnal cycle in the MC can weaken the MJO
622 and its eastward propagation (Hagos et al., 2016; Oh et al., 2013). We conducted an
623 experiment to determine whether computing surface heat fluxes using daily mean
624 values, instead of instantaneous values, of atmospheric variables and SST with the
625 same coupling frequency would affect the MJO simulation. The coupling in the model
626 was conducted through the SHF and LHF exchange between the atmosphere and
627 ocean, that were calculated based on simulated winds, moisture, and temperature. As
628 mentioned in Section 2.3, air–sea fluxes were calculated twice for every time step
629 (coupling 48 times per day) in the control coupled experiment (C–30NS) based on the
630 instantaneous values of atmospheric and oceanic variables. In the experiment in which
631 the diurnal cycle was removed (C–30NS–nD), air–sea fluxes were calculated as in C–
632 30NS but were based on daily means of both atmospheric variables and SST. Doing

Deleted: 7

Deleted: 7c

Deleted: 7d

Deleted: 7g

Deleted: 7h

Deleted: 7k

Deleted: 7l

Deleted: 7k

Deleted: 7l

Deleted: 8c

Deleted: 8d

644 this removed certain diurnal effects of air-sea coupling. The results shown in Fig. 10
645 reveal the enhancement of the eastward-propagating signals in the MJO (e.g., a larger
646 amplitude in spectrum; Fig. 10a) and further eastward propagation (Fig. 10b) as well
647 stronger coupling between precipitation and SST (Fig. 10c) in C-30NS-nD. The
648 overall results are consistent with previous finding that the diurnal cycle tends to
649 reduce the amplitude of the MJO, indicating that the weakening effect occurs through
650 air-sea coupling in addition to those processes in the atmosphere. Previous studies
651 have hypothesized that rapid interaction processes in the diurnal time scale tend to
652 extract energy from the MJO, thus reducing the strength and propagation tendency of
653 the MJO. However, a comparison between the spectra of C-30NS and C-30NS-nD
654 indicates that the experiment in which the diurnal cycle is removed appeared to
655 oversimulate the MJO with unrealistic strength, suggesting that the effect of the
656 diurnal cycle should be considered in the model to simulate a more realistic MJO.
657 However, whether this is a common result in different models remain to be examined.

Deleted: 9

Deleted: 9a

Deleted: 9b

Deleted: 9c

659 4. Discussion and conclusions

660 Air-sea coupling is a key mechanism for the successful simulation of the MJO
661 (Chang et al., 2019; DeMott et al., 2015; Jiang et al., 2015, 2020; Kim et al., 2010; Li
662 et al., 2016; Li et al., 2020; Newman et al., 2009; Tseng et al., 2014). This study,
663 following the study of Tseng et al. (2014), demonstrated that coupling a high-
664 resolution 1-D TKE ocean model (namely the SIT model) to the CAM5, namely the
665 CAM5-SIT, significantly improved the MJO simulation over the standalone CAM5.
666 By coupling SIT model to an AGCM different from Tseng et al. (2014), this study
667 confirms the scientific reproducibility for the improvement of MJO simulation in
668 modeling science. The CAM5-SIT realistically simulates the MJO characteristics in
669 many aspects (e.g., intraseasonal periodicity, eastward propagation, coherence in the

674 low-frequency band, detouring propagation across the MC, tilting vertical structure,
675 and intraseasonal variance in the WP).

676 Systematic sensitivity experiments were conducted to investigate the effects of
677 the vertical resolution and the thickness of the 1-D ocean model, coupling domains,
678 and the absence of the diurnal cycle. The results of all the sensitivity experiments are
679 summarized in Fig. [11a](#) and [11b](#), which show four common metrics for MJO
680 evaluation. The four metrics are the propagation speed of the MJO (estimated from
681 the U850 Hovmöller diagram as Fig. 2d–f) versus the power ratio of eastward- and
682 westward-propagating 30–80-day signals (E/W ratio, derived from the zonal W–FS)
683 in Fig. [11a](#) and the eastward propagation speed of the 30–80-day filtered precipitation
684 anomaly (estimated from the precipitation Hovmöller diagram) versus the variance
685 explained by RMM1 and RMM2 (i.e., the sum of the variance explained by [the first](#)
686 [two empirical orthogonal functions](#) (EOF1 and EOF2) based on Wheeler and Hendon,
687 2004) in Fig. [11b](#). Based on the maximum precipitation anomaly and zero values of
688 U850 (indicating deep convection region), propagation speeds of precipitation and
689 U850 were calculated from Hovmöller diagrams between 60°E and 150°W. Overall,
690 the control experiment C–30NS simulates the most realistic MJO among all
691 sensitivity experiments.

692 As for vertical resolution, we determined that the MJO simulation efficiency
693 decreased when the vertical resolution of the SIT model is decreased from 1 m to [11.5](#)
694 or [33.9](#) m, as simulated in the C–LR12m and C–LR34m experiments, respectively.
695 This finding, consistent with that reported by Tseng et al. (2014), suggests that a finer
696 vertical resolution more effectively resolves temperature variations in the ocean warm
697 layer and enhances atmospheric–ocean coupling, thus enabling the upper ocean to
698 more efficiently respond to atmospheric forcing by providing sensible and latent heat
699 fluxes; this results in superior synchronization between the lower atmosphere and the

Deleted: 10a

Deleted: 10b

Deleted: 10a

Deleted: 10b

Deleted: 12

Deleted: 34

706 upper ocean.

707 We observed that the shallower ocean model bottom could speed up the eastward
708 propagation of the MJO by producing more perturbations of shorter periodicity (Fig.

709 7) and results in a weaker MJO. The shallower ocean layer with vertical grids likely

710 responds more quickly to atmospheric forcing but provides less sensible and latent

711 heat fluxes to the atmosphere. Thus, the MJO propagates too fast with a weaker

712 amplitude.

713 In the coupling domain sensitivity experiments, we investigated the essential
714 coupling domain required to simulate the realistic MJO and the effect of the domain
715 on the MJO simulation. Coupling only the northern tropics fails to simulate the
716 eastward propagation, whereas coupling only the southern tropics yields a more
717 realistic MJO simulation, although this simulation is inferior to coupling the entire
718 tropics. This contrast reveals the importance of the southern tropical ocean, especially
719 in the MC where high SST and moisture content are noted. Coupling in the southern
720 tropics is therefore essential for providing the energy required to maintain the MJO
721 and its eastward propagation. By contrast, the northern tropics are relatively dry and
722 cool. Coupling in this region is therefore less effective in improving MJO simulation.

723 In the longitudinal domain sensitivity experiments, we found that the MJO
724 amplitude and the eastward extend of its eastward propagation are enhanced by
725 extending the eastern boundary of the coupling domain from the tropical eastern IO to
726 the tropical WP and further to the tropical eastern Pacific (Fig. 1). Further extension
727 of the domain to cover the tropical Atlantic does not exhibit further enhancement (not
728 shown). This result indicates that coupling in the tropical central and eastern Pacific,
729 although not the major MJO signal regions (i.e., from the tropical IO to the tropical
730 WP), still played a marked role in sustaining the MJO. We propose the following to
731 explain this effect. Because of the planetary scale of the MJO, the near-surface

Deleted: 6

Deleted: oceanic mixed

734 easterly circulation to the east of the convection core often extended to the tropical
735 central and eastern Pacific where the climatological easterly prevailed. The coupling
736 beyond the WP increased low-level moisture transport and convergence to the east of
737 the convection and establish an environment suitable for the further eastward
738 propagation of the MJO. This effect was likely terminated by the landmass of Central
739 America when the tropical Atlantic was further included. Thus, a further eastward
740 extension of the coupling domain exerted little effect on further enhancing the MJO. A
741 diagnostic study on the effect of the longitudinal coupling domain is being conducted,
742 and the results will be reported in a following paper.

743 The diurnal versus nondiurnal cycle experiment indicates that nondiurnal
744 coupling tended to enhance eastward-propagating signals but slow down the eastward
745 propagation (Fig. 11a–b). This result is consistent with the finding of previous studies
746 that the diurnal cycle in the atmosphere extracts energy from the MJO, thus
747 weakening it.

748 In this study, we demonstrated how air–sea coupling can improve the MJO
749 simulation in a GCM. The findings are as follows.

750 (1) Better resolving the fine structure of the upper-ocean temperature and therefore
751 the air–sea interaction leads to more realistic intraseasonal variability in both
752 tropical SST and atmospheric circulation.

753 (2) An adequate thickness of vertically-gridded upper ocean is required to simulate a
754 delayed response of the upper ocean to atmospheric forcing and lower-frequency
755 fluctuation.

756 (3) Coupling the tropical eastern Pacific, in addition to the tropical IO and the tropical
757 WP, can enhance the MJO and facilitate the further eastward propagation of the
758 MJO to the dateline.

759 (4) Coupling the southern tropical ocean, instead of the norther tropical ocean, is

Deleted: 10a

Deleted: the oceanic mixed layer

762 essential for simulating a realistic MJO.

763 (5) Stronger MJO variability can be obtained without considering the diurnal cycle in
764 coupling.

765 Our study confirmed the effectiveness of air–sea coupling for improving MJO
766 simulation in a climate model and demonstrated how and where to couple. The
767 findings enhance our understanding of the physical processes that shape the
768 characteristics of the MJO.

769

770 *Code and data availability.* The model code of CAM5–SIT is available at
771 <https://doi.org/10.5281/zenodo.5510795>. Input data of CAM5–SIT using the
772 climatological Hadley Centre Sea Ice and Sea Surface Temperature dataset and
773 GODAS data forcing, including 30-year numerical experiments, are available at
774 <https://doi.org/10.5281/zenodo.5510795>.

775

776 *Author contributions.* HHH is the initiator and the primary investigator of the
777 Taiwan Earth System Model project. YYL is the CAM5–SIT model developer and
778 writes the majority part of the paper. WLT and LCJ assist in MJO analysis.

779

780 *Competing interests.* The authors declare that they have no conflict of interest.

781

782 *Acknowledgements.* The contribution from YYL, HHH, WLT, and LCJ to this study is
783 supported by Ministry of Science and Technology of Taiwan under contracts MOST
784 110-2123-M-001-003, MOST 110-2811-M-001-603, MOST 109-2811-M-001-624
785 and MOST108-2811-M-001-643. Our deepest gratitude goes to the editors and
786 anonymous reviewers for their careful work and thoughtful suggestions that have
787 helped improve this paper substantially. We sincerely thank the National Center for

788 Atmospheric Research and their Atmosphere Model Working Group (AMWG) for
789 release CESM1.2.2. We thank the computational support from National Center for
790 High530 performance Computing of Taiwan. This manuscript was edited by Wallace
791 Academic Editing.

792

793 **Reference**

- 794 Adler, R. F., Huffman, G. J., Chang, A., Ferraro, R., Xie, P.
795 P., Janowiak, J., Rudolf, B., Schneider, U., Curtis, S., Bolvin,
796 D., Gruber, A., Susskind, J., Arkin, P., and Nelkini, E.: The
797 Version 2.1 Global Precipitation Climatology Project (GPCP)
798 Monthly Precipitation Analysis (1979 -Present), *J. Hydrometeor.*,
799 4(6), 1147-1167, [https://doi.org/10.1175/1525-](https://doi.org/10.1175/1525-7541(2003)004<1147:TVGPCP>2.0.CO;2)
800 7541(2003)004<1147:TVGPCP>2.0.CO;2, 2003.
- 801 Ahn, M.-S., Kim, D., Kang, D., Lee, J., Sperber, K. R., and Glecker, P.
802 J., et al.: MJO propagation across the Maritime Continent: Are
803 CMIP6 models better than CMIP5 models? *Geophys. Res. Lett.*, 47,
804 e2020GL087250, <https://doi.org/10.1029/2020GL087250>, 2020.
- 805 Ahn, M.-S., Kim, D., Sperber, K. R., Kang, I.-S., Maloney, E., Waliser,
806 D., and Hendon, H.: MJO simulation in CMIP5 climate models:
807 MJO skill metrics and process-oriented diagnosis, *Clim.*
808 *Dyn.*, 49, 4023–4045, <https://doi.org/10.1007/s00382-017-3558-4>,
809 2017.
- 810 Alappattu, D. P., Wang, Q., Kalogiros, J., Guy, N., and Jorgensen, D.
811 P.: Variability of upper ocean thermohaline structure during a MJO
812 event from DYNAMO aircraft observations, *J. Geophys. Res. -*
813 *Oceans*, 122, 1122–1140, <https://doi.org/10.1002/2016JC012137>,
814 2017.
- 815 Amante, C., and Eakins, B. W.: ETOPO1 1 arc-minute globe relief
816 model: Procedures, data sources and analysis, NOAA Tech. Memo.
817 NESDIS NGDC-24, 19 pp., NOAA, Silver Spring, Md., 2009.
- 818 Behringer, D. W., and Xue, Y.: Evaluation of the global ocean data
819 assimilation system at NCEP: The Pacific Ocean. Eighth
820 Symposium on Integrated Observing and Assimilation Systems for
821 Atmosphere, Oceans, and Land Surface, AMS 84th Annual
822 Meeting, Washington State Convention and Trade Center, Seattle,
823 Washington, 11-15. Derber, J.C., and A. Rosati, 1989: A global
824 oceanic data assimilation system, *J. Phys. Oceanogr.*, 19, 1333–
825 1347, <https://ams.confex.com/ams/pdfpapers/70720.pdf>, 2004.
- 826 Bentsen, M., Bethke, I., Debernard, J. B., Iversen, T., Kirkevåg, A.,
827 Seland, Ø., Drange, H., Roelandt, C., Seierstad, I. A., Hoose, C.,
828 and Kristjánsson, J. E.: The Norwegian Earth System Model,
829 NorESM1-M – Part 1: Description and basic evaluation of the

- 830 physical climate, *Geosci. Model Dev.*, 6, 687–720,
831 <https://doi.org/10.5194/gmd-6-687-2013>, 2013.
- 832 Bernie, D., Guilyardi, E., Madec, G., Slingo, J., Woolnough, S., and
833 Cole, J.: Impact of resolving the diurnal cycle in an ocean–
834 atmosphere GCM. Part 2: a diurnally coupled CGCM, *Clim.*
835 *Dynam.*, 31, 909–925, <https://doi.org/10.1007/s00382-008-0429-z>,
836 2008.
- 837 Boyle, J. S., Klein, S. A., Lucas, D. D., Ma, H.-Y., Tannahill, J., and
838 Xie, S.: The parametric sensitivity of CAM5’s MJO, *J. Geophys.*
839 *Res.-Atmos.*, 120, 1424–1444,
840 <https://doi.org/10.1002/2014JD022507>, 2015.
- 841 Bui, H. X., and Maloney, E. D.: Changes in Madden-Julian Oscillation
842 precipitation and wind variance under global warming, *Geophys.*
843 *Res. Lett.*, 45, 7148–7155, <https://doi.org/10.1029/2018GL078504>,
844 2018.
- 845 Chang, M.-Y., Li, T., Lin, P.-L., and Chang, T.-H.: Forecasts of MJO
846 Events during DYNAMO with a Coupled Atmosphere-Ocean
847 Model: Sensitivity to Cumulus Parameterization Scheme, *J.*
848 *Meteorol. Res.*, 33, 1016–1030, [https://doi.org/10.1007/s13351-](https://doi.org/10.1007/s13351-019-9062-5)
849 [019-9062-5](https://doi.org/10.1007/s13351-019-9062-5), 2019.
- 850 CLIVAR MADDEN–JULIAN OSCILLATION WORKING GROUP:
851 MJO simulation diagnostics, *J. Climate*, 22, 3006–3030,
852 <https://doi.org/10.1175/2008JCLI2731.1>, 2009.
- 853 Crueger, T., Stevens, B., and Brokopf, R.: The Madden–Julian
854 Oscillation in ECHAM6 and the introduction of an objective MJO
855 metric, *J. Climate*, 26, 3241–3257, [https://doi.org/10.1175/JCLI-D-](https://doi.org/10.1175/JCLI-D-12-00413.1)
856 [12-00413.1](https://doi.org/10.1175/JCLI-D-12-00413.1), 2013.
- 857 Danabasoglu, G., Lamarque, J.-F., Bacmeister, J., Bailey, D. A.,
858 DuVivier, A. K., and Edwards, J., et al.: The Community Earth
859 System Model Version 2 (CESM2), *J. Adv. Model. Earth Syst.*, 12,
860 e2019MS001916, <https://doi.org/10.1029/2019MS001916>, 2020.
- 861 Dee, D. P., Uppala, S. M., Simmons, A. J., Berrisford, P., Poli, P.,
862 Kobayashi, S., Andrae, U., Balmaseda, M. A., Balsamo, G., Bauer,
863 P., Bechtold, P., Beljaars, A. C. M., van de Berg, L., Bidlot, J.,
864 Bormann, N., Delsol, C., Dragani, R., Fuentes, M., Geer, A. J.,
865 Haimberger, L., Healy, S. B., Hersbach, H., Hólm, E. V., Isaksen,
866 L., Kållberg, P., Köhler, M., Matricardi, M., McNally, A. P.,
867 Monge-Sanz, B. M., Morcrette, J.-J., Park, B.-K., Peubey, C., de
868 Rosnay, P., Tavolato, C., Thépaut, J.-N., and Vitart, F.: The ERA-
869 Interim reanalysis: configuration and performance of the data
870 assimilation system, *Q. J. R. Meteorol. Soc.*, 137: 553–597,
871 <https://doi.org/10.1002/qj.828>, 2011.
- 872 de Szoeki, S. P., Skillingstad, E. D., Zuidema, P., and Chandra, A.
873 S.: Cold pools and their influence on the tropical marine boundary

- 874 layer, *J. Atmos. Sci.*, 74, 1149–1168. <https://doi.org/10.1175/JAS->
875 [D-16-0264.1](https://doi.org/10.1175/JAS-D-16-0264.1), 2017.
- 876 Delworth, T. L., et al.: GFDL's CM2 global coupled climate models.
877 Part 1: Formulation and simulation characteristics, *J. Climate*, 19,
878 643–674, <https://doi.org/10.1175/JCLI3629.1>, 2006.
- 879 DeMott, C. A., Klingaman, N. P., and Woolnough, S. J.: Atmosphere-
880 ocean coupled processes in the Madden-Julian oscillation, *Rev.*
881 *Geophys.*, 53, 1099–1154, <https://doi.org/10.1002/2014RG000478>,
882 2015.
- 883 DeMott, C. A., Klingaman, N. P., Tseng, W.-L., Burt, M. A., Gao, Y.,
884 and Randall, D. A.: The convection connection: How ocean
885 feedbacks affect tropical mean moisture and MJO propagation, *J.*
886 *Geophys. Res.-Atmos.*, 124, 11,910–11,931,
887 <https://doi.org/10.1029/2019JD031015>, 2019.
- 894 Haertel, P.: Prospects for Erratic and Intensifying Madden-Julian
895 Oscillations, *Climate*, 8, 24, <https://doi.org/10.3390/cli8020024>,
896 2020.
- 897 Hannah, W. M., and Maloney, E. D.: The moist static energy budget in
898 NCAR CAM5 hindcasts during DYNAMO, *J. Adv. Model. Earth*
899 *Syst.*, 6, 420–440, <https://doi.org/10.1002/2013MS000272>, 2014.
- 900 Hagos, S. M., Zhang, C., Feng, Z., Burleyson, C. D., Mott, C. De,
901 Kerns, B., Benedict, J. J., and Martini, M. N.: The impact of the
902 diurnal cycle on the propagation of Madden-Julian Oscillation
903 convection across the Maritime Continent, *J. Adv. Model. Earth*
904 *Syst.*, 8, 1552–1564, <https://doi.org/10.1002/2016MS000725>, 2016.
- 905 He, S., Yang, S., and Li, Z.: Influence of Latent Heating over the Asian
906 and Western Pacific Monsoon Region on Sahel Summer
907 Rainfall, *Sci. Rep.* 7, 7680, <https://doi.org/10.1038/s41598-017->
908 [07971-6](https://doi.org/10.1038/s41598-017-07971-6), 2017.
- 909 Heath, A., Gonzalez, A. O., Gehne, M., and Jaramillo, A.: Interactions
910 of large-scale dynamics and Madden-Julian Oscillation propagation
911 in multi-model simulations, *J. Geophys. Res.-Atmos.*, 126,
912 e2020JD033988. <https://doi.org/10.1029/2020JD033988>, 2021.
- 913 Hong, X., Reynolds, C. A., Doyle, J. D., May, P., and O'Neill, L.:
914 Assessment of upper-ocean variability and the Madden-Julian
915 Oscillation in extended-range air–ocean coupled mesoscale
916 simulations, *Dyn. Atmos. Oceans*, 78, 89–105.
917 <https://doi.org/10.1016/j.dynatmoce.2017.03.002>, 2017.
- 918 Hung, M.-P., Lin, J.-L., Wang, W., Kim, D., Shinoda, T., and Weaver,
919 S. J.: MJO and convectively coupled equatorial waves simulated by
920 CMIP5 climate models, *J. Climate*, 26, 6185–6214,
921 <https://doi.org/10.1175/JCLI-D-12-00541.1>, 2013.
- 922 Hurrell, J. W., Holland, M. M., Gent, P. R., Ghan, S., Kay, J. E.,

- 923 Kushner, P. J., Lamarque, J.-F., Large, W. G., Lawrence, D.,
 924 Lindsay, K., Lipscomb, W. H., Long, M. C., Mahowald, N., Marsh,
 925 D. R., Neale, R. B., Rasch, P., Vavrus, S., Vertenstein, M., Bader,
 926 D., Collins, W. D., Hack, J. J., Kiehl, J., and Marshall, S.: The
 927 community Earth system model: A framework for collaborative
 928 research, *B. Am. Meteorol. Soc.*, 94, 1319–1360,
 929 <https://doi.org/10.1175/BAMS-D-12-00121>, 2013.
- 930 Jiang, X., et al.: Vertical structure and physical processes of the
 931 Madden-Julian oscillation: Exploring key model physics in climate
 932 simulations, *J. Geophys. Res.-Atmos.*, 120, 4718–4748,
 933 <https://doi.org/10.1002/2014JD022375>, 2015.
- 934 Jiang, X., Adames, Á. F., Kim, D., Maloney, E. D., Lin, H., and Kim,
 935 H., et al.: Fifty years of research on the Madden-Julian Oscillation:
 936 Recent progress, challenges, and perspectives, *J. Geophys. Res.-*
 937 *Atmos.*, 125, e2019JD030911,
 938 <https://doi.org/10.1029/2019JD030911>, 2020.
- 939 Johnson, R. H., and Ciesielski, P. E.: Multiscale variability of the
 940 atmospheric boundary layer during DYNAMO, *J. Atmos.*
 941 *Sci.*, 74, 4003–4021, <https://doi.org/10.1175/JAS-D-17-0182.1>,
 942 2017.
- 943 Kaylor, R. E.: Filtering and decimation of digital time series, *Tech.*
 944 *Rep. Note BN 850*, Institute for Physical Science and Technology,
 945 University of Maryland at College Park, 14 pp., 1977.
- 946 Kim, D., Sobel, A. H., Maloney, E. D., Frierson, D. M., and Kang, I.-
 947 S.: A systematic relationship between intraseasonal variability and
 948 mean state bias in AGCM simulations, *J. Climate*, 24, 5506–5520.
 949 <https://doi.org/10.1175/2011JCLI4177.1>, 2011.
- 950 Kim, D., Kim H., and Lee, M.-I.: Why does the MJO detour the
 951 Maritime Continent during austral summer? *Geophys. Res. Lett.*,
 952 44, 2579–2587, <https://doi.org/10.1002/2017GL072643>, 2017.
- 953 Kim, H.-M., Hoyos, C. D., and Webster, P. J. et al.: Ocean–atmosphere
 954 coupling and the boreal winter MJO, *Clim Dynam.*, 35, 771–784,
 955 <https://doi.org/10.1007/s00382-009-0612-x>, 2010.
- 956 Kiranmayi, L., and Maloney, E. D.: Intraseasonal moist static energy
 957 budget in reanalysis data, *J. Geophys. Res.*, 116, D21117,
 958 <https://doi.org/10.1029/2011JD016031>, 2011.
- 959 Lan, Y.-Y., Tsuang, B.-J., Tu, C.-Y., Wu, T.-Y., Chen, Y.-L., and
 960 Hsieh, C.-I.: Observation and Simulation of Meteorology and
 961 Surface Energy Components over the South China Sea in Summers
 962 of 2004 and 2006, *Terr. Atmos. Ocean. Sci.*, 21, 325–342,
 963 [https://doi.org/10.3319/TAO.2009.04.07.01\(A\)](https://doi.org/10.3319/TAO.2009.04.07.01(A)), 2010.
- 964 Lee, H.-T., and NOAA CDR Program: NOAA Climate Data Record
 965 (CDR) of Daily Outgoing Longwave Radiation (OLR), Version 1.2,
 966 NOAA National Climatic Data

- 967 Center, <https://doi.org/10.7289/V5SJ1HH2>, 2011.
- 968 Li, T., Ling, J., and Hsu, P.-C.: Madden–Julian Oscillation: Its
969 discovery, dynamics, and impact on East Asia, *J. Meteor. Res.*, 34,
970 20–42, <https://doi.org/10.1007/s13351-020-9153-3>, 2020.
- 971 Li, T., Tam, F., Fu, X., Zhou, T., and Zhu, W.: Causes of the
972 intraseasonal SST variability in the tropical Indian Ocean, *Atmos.*
973 *Oceanic Sci. Lett.*, 1, 18–23,
974 <https://doi.org/10.1080/16742834.2008.11446758>, 2008.
- 975 Li, X., Tang, Y., Zhou, L., Chen, D., and Yao, Z.: Assessment of Madden–Julian
976 oscillation simulations with various configurations of CESM, *Clim. Dynam.*,
977 47, 2667–2690, <https://doi.org/10.1007/s00382-016-2991-0>, 2016.
- 978 Ling, J., Zhao, Y., and Chen, G.: Barrier effect on MJO propagation by
979 the Maritime Continent in the MJO Task Force/GEWEX
980 atmospheric system study models, *J. Climate*, 32, 5529–
981 5547, <https://doi.org/10.1175/JCLI-D-18-0870.1>, 2019.
- 982 Madden, R. A., and Julian, P. R.: Description of global-scale
983 circulation cells in the tropics with a 40–50 day period, *J. Atmos.*
984 *Sci.*, 29, 1109–1123, [https://doi.org/10.1175/1520-0469\(1972\)029<1109:DOGSCC>2.0.CO;2](https://doi.org/10.1175/1520-0469(1972)029<1109:DOGSCC>2.0.CO;2), 1972.
- 986 Madden, R. A., and Julian, P. R.: Observations of the 40–50 day
987 tropical oscillation - A review, *Mon. Weather Rev.*, 122, 814– 837,
988 [https://doi.org/10.1175/1520-0493\(1994\)122<0814:OOTDIO>2.0.CO;2](https://doi.org/10.1175/1520-0493(1994)122<0814:OOTDIO>2.0.CO;2), 1994.
- 990 Neale, R. B., et al.: Description of the NCAR Community Atmosphere
991 Model (CAM 5.0), NCAR Tech. Note NCAR/TN-486+STR, 289
992 pp., Natl. Cent. for Atmos. Res, Boulder, Colo., 2012.
- 993 Newman, M., Sardeshmukh, P. D., and Penland, C.: How important is
994 air–sea coupling in ENSO and MJO evolution? *J.*
995 *Clim.*, 22, 2958– 2977, <https://doi.org/10.1175/2008JCLI2659.1>,
996 2009.
- 997 Oh, J., Kim, B., and Kim, K. et al.: The impact of the diurnal cycle on
998 the MJO over the Maritime Continent: a modeling study
999 assimilating TRMM rain rate into global analysis, *Clim.*
1000 *Dynam.*, 40, 893–911, <https://doi.org/10.1007/s00382-012-1419-8>,
1001 2013.
- 1002 Pei, S., Shinoda, T., Soloviev, A., and Lien, R.-C.: Upper ocean
1003 response to the atmospheric cold pools associated with the
1004 Madden-Julian Oscillation, *Geophys. Res. Lett.*, 45, 5020–5029,
1005 <https://doi.org/10.1029/2018GL077825>, 2018.
- 1006 Pujiana, K., Moum, J. N., and Smyth, W. D.: The role of subsurface
1007 turbulence in redistributing upper-ocean heat, freshwater, and
1008 momentum in response to the MJO in the equatorial Indian
1009 Ocean, *J. Phys. Oceanogr.*, 48, 197–

- 1010 220, <https://doi.org/10.1175/JPO-D-17-0146.1>, 2018.
- 1011 Rayner, N. A., Parker, D. E., Horton, E. B., Folland, C. K., Alexander,
1012 L. V., Rowell, D. P., Kent, E. C., and Kaplan, A.: Global analyses
1013 of sea surface temperature, sea ice, and night marine air
1014 temperature since the late nineteenth century, *J. Geophys. Res.*,
1015 108(D14), 4407, <https://doi.org/10.1029/2002JD002670>, 2003.
- 1016 Ren, P. F., Gao, L., and Ren, H.-L. et al.: Representation of the
1017 Madden–Julian Oscillation in CAMSCSM, *J. Meteor. Res.*, 33,
1018 627–650, <https://doi.org/10.1007/s13351-019-8118-x>, 2019.
- 1019 Reynolds, R. W., and Smith, T. M.: A high-resolution global sea
1020 surface temperature climatology, *J. Clim.*, 8(6),1571–1583,
1021 <https://doi.org/10.1175/1520->
1022 0442(1995)008<1571:AHRGSS>2.0.CO;2, 1995.
- 1023 Schreck, C. J., Lee, H.-T., and Knapp, K. R.: HIRS outgoing longwave
1024 radiation—Daily climate data record: Application toward
1025 identifying tropical subseasonal variability, *Remote Sens.*, 10,
1026 1325. <https://doi.org/10.3390/rs10091325>, 2018.
- 1027 Sobel, A. H., Maloney, E. D., Bellon, G., and Dargan, M. F.: The role
1028 of surface heat fluxes in tropical intraseasonal oscillations, *Nat.*
1029 *Geosci.*, 1, 653–657, <https://doi.org/10.1038/ngeo312>, 2008.
- 1030 Subramanian, A. C., Jochum, M., Miller, A. J., Murtugudde, R., Neale,
1031 R. B., and Waliser, D. E.: The Madden–Julian oscillation in
1032 CCSM4, *J. Climate*, 24, 6261–6282, <https://doi.org/10.1175/JCLI->
1033 D-11-00031.1, 2011.
- 1034 Tseng, W.-L., Tsuang, B.-J., Keenlyside, N. S., Hsu, H.-H. and Tu, C.-
1035 Y.: Resolving the upper-ocean warm layer improves the simulation
1036 of the Madden-Julian oscillation, *Clim. Dynam.*, 44, 1487–1503,
1037 <https://doi.org/10.1007/s00382-014-2315-1>, 2014.
- 1038 Tseng, W.-L., Hsu, H.-H., Keenlyside, N., Chang, C.-W. J., Tsuang,
1039 B.-J., Tu, C.-Y., and Jiang, L.-C.: Effects of Orography and Land–
1040 Sea Contrast on the Madden–Julian Oscillation in the Maritime
1041 Continent: A Numerical Study Using ECHAM-SIT, *J. Climate*, 30,
1042 9725–9741, <https://doi.org/10.1175/JCLI-D-17-0051.1>, 2017.
- 1043 Tu, C.-Y., and Tsuang, B.-J.: Cool-skin simulation by a one-column
1044 ocean model, *Geophys. Res. Lett.*, 32, L22602,
1045 <https://doi.org/10.1029/2005GL024252>, 2005.
- 1046 Wang, W., Saha, S., Pan, H.-L., Nadiga, S., and White, G.: Simulation
1047 of ENSO in the new NCEP Coupled Forecast System Model
1048 (CFS03), *Mon. Wea. Rev.*, 133, 1574–1593,
1049 <https://doi.org/10.1175/MWR2936.1>, 2005.
- 1050 Wang, W., Hung, M.-P., Weaver, S. J., Kumar, A., and Fu, X.: MJO
1051 prediction in the NCEP Climate Forecast System version 2, *Clim.*
1052 *Dyn.*, 42, 2509–2520, <https://doi.org/10.1007/s00382-013-1806-9>,

- 1053 2014.
- 1054 Wheeler, M. C., and Hendon, H. H.: An all-season real-time
1055 multivariate MJO index: development of an index for monitoring
1056 and prediction, *Mon. Weather Rev.*, 132, 1917–1932,
1057 [https://doi.org/10.1175/1520-](https://doi.org/10.1175/1520-0493(2004)132<1917:AARMMI>2.0.CO;2)
1058 [0493\(2004\)132<1917:AARMMI>2.0.CO;2](https://doi.org/10.1175/1520-0493(2004)132<1917:AARMMI>2.0.CO;2), 2004.
- 1059 Wheeler, M., and Kiladis, G. N.: Convectively coupled equatorial
1060 waves: Analysis of clouds and temperature in the wavenumber-
1061 frequency domain, *J. Atmos. Sci.*, 56, 374– 399,
1062 [https://doi.org/10.1175/1520-](https://doi.org/10.1175/1520-0469(1999)056<0374:CCEWAO>2.0.CO;2)
1063 [0469\(1999\)056<0374:CCEWAO>2.0.CO;2](https://doi.org/10.1175/1520-0469(1999)056<0374:CCEWAO>2.0.CO;2), 1999.
- 1064 Woolnough, S. J., Vitard, F., and Balmaseda, M. A.: The role of the
1065 ocean in the Madden–Julian oscillation: Implications for MJO
1066 prediction, *Quart. J. Roy. Meteor. Soc.*, 133, 117–128,
1067 <https://doi.org/10.1002/qj.4>, 2007.
- 1068 Wu, C.-H., and Hsu, H.-H.: Potential Influence of Topography on the
1069 MJO in the Maritime Continent, *J. Climate*, 22, 5433–5448,
1070 <https://doi.org/10.1175/2009JCLI2825.1>, 2009.
- 1071 Yoneyama, K., Zhang, C., and Long, C.: Tracking pulses of the
1072 Madden–Julian oscillation, *Bull. Amer. Meteor. Soc.*, 94, 1871–
1073 1891, <https://doi.org/10.1175/BAMS-D-12-00157.1>, 2013.
- 1074 Zhang, C.: Madden-Julian oscillation, *Rev. Geophys.*, 43, RG2003,
1075 <https://doi.org/10.1029/2004RG000158>, 2005.
- 1076 Zhang, C., and Yoneyama, K.: CINDY/DYNAMO field campaign:
1077 Advancing our understanding of MJO initiation, In *World
1078 Scientific Series on Asia-Pacific Weather and Climate* (pp. 339-
1079 348). (*World Scientific Series on Asia-Pacific Weather and
1080 Climate; Vol. Volume 9*), World Scientific Publishing Co. Pte Ltd.
1081 https://doi.org/10.1142/9789813200913_0027, 2017.

1082 Table 1. List of experiments

Section	Category	Experiments	Description
3.1	Coupled or uncoupled	A-CTL	Standalone CAM5.3 forced by forced by the monthly mean Hadley Centre SST dataset version 1 climatology
		C-30NS (the control coupled experiment)	CAM5.3 coupled with SIT over the tropical domain (30°N-30°S), with 41 layers of finest vertical resolution (up to the seabed) and diurnal cycle; the frequency of CAM5 being exchanged with CPL is 48 times per day
3.2	Upper-ocean vertical resolution	C-LR12m	The first ocean vertical level starts at 11.5 m with 31 layers (beside SST and cool skin layer are 11.5 m, 29.5 m and 43.6 m up to the seabed)
		C-LR34m	The first ocean vertical level starts at 33.9 m with 28 layers (beside SST and cool skin layer are 33.9 m, 76.9 m and 96.8 m up to the seabed)
3.3	Lowest boundary of SIT	C-HR1mB10m	The lowest boundary of SIT has a depth of 10 m (model depth between 0 m and 10 m)
		C-HR1mB30m	The lowest boundary of SIT has a depth of 30 m (model depth between 0 m and 30 m)
		C-HR1mB60m	The lowest boundary of SIT has a depth of 60 m (model depth between 0 m and 60 m)
3.4	Regional coupling domain in latitude	C-0_30N	Coupled in the tropical northern hemisphere (0°N-30°N, 0°E-360°E)
		C-0_30S	Coupled in the tropical southern hemisphere (0°S-30°S, 0°E-360°E)
	Regional coupling domain in longitude	C-30_180E	Coupled in the Indo-Pacific (30°N-30°S, 30°E-180°E)
		C-30E_75W	Coupled over the Indian Ocean and Pacific Ocean (30°N-30°S, 30°E-75°W)
3.5	Absence of the diurnal cycle	C-30NS-nD	Absence of the diurnal cycle in C-30NS; the CAM5.3 daily atmospheric mean of surface wind, temperature, total precipitation, net surface heat flux, u-stress and v-stress over water trigger the SIT and daily mean SST feedback to atmosphere; the frequency of CAM5 is exchanged with CPL 48 times per day

1083 Experiment abbreviations: “A” means standalone AGCM simulation. “C” means the
 1084 CAM5.3 coupled to the SIT model.

1085 **Figure List**

1086 **Figure 1.** Schematics of coupled and uncoupled domains in the regional coupling
1087 experiment: (a) C-30NS, (b) C-0_30N, (c) C-0_30S, (d) C-30_180E, and (e) C-
1088 30E_75W. The background is the climatological mean SST in December–February (DJF).
1089

1090 **Figure 2.** (a)–(c) Zonal wavenumber–frequency spectra for 850-hPa zonal wind averaged
1091 over 10°S–10°N in boreal winter after removing the climatological mean seasonal cycle.
1092 Vertical dashed lines represent periods at 80 and 30 days, respectively. (d)–(f) Hovmöller
1093 diagrams of the correlation between the precipitation averaged over 10°S–5°N, 75–100°E
1094 and the intraseasonally filtered precipitation (color) and 850-hPa zonal wind (contour)
1095 averaged over 10°N–10°S. (g)–(i) Zonal wavenumber–frequency power spectra of
1096 anomalous OLR (colors) and phase lag with U850 (vectors) for the symmetric component
1097 of tropical waves, with the vertically upward vector representing a phase lag of 0° with
1098 phase lag increasing clockwise. Three dispersion straight lines with increasing slopes
1099 represent the equatorial Kelvin waves (derived from the shallow water equations)
1100 corresponding to three equivalent depths, 12, 25, and 50 m, respectively. (j)–(l)
1101 Composites of 20–100-day filtered OLR ($W m^{-2}$, shaded) and 850-hPa wind ($m s^{-1}$,
1102 vector) for MJO phase 5 when deep convection is the strongest over the MC and 850-hPa
1103 wind, with the reference vector ($1 m s^{-1}$) shown at the top right of each panel, and (m)–
1104 (o) 15°N–15°S averaged p-vertical velocity anomaly ($Pa s^{-1}$, shaded) and moist static
1105 energy tendency anomaly ($W m^{-2}$, contour, interval 0.003); solid, dashed, and thick-black
1106 lines represent positive, negative, and zero values, respectively. The number of days used
1107 to generate the composite is shown at the bottom right corner of each panel. (a), (d), (g),
1108 (j), and (m) are from the ERA-Interim and NOAA post-processed data (abbr. ERA-
1109 I/NOAA); (b), (e), (h), (k), and (n) are from the control experiment C-30NS; and (c), (f),
1110 (i), (l), and (o) are from the A-CTL.

1111
1112 **Figure 3.** Evolution of the filtered OLR anomaly ($W m^{-2}$, shaded) and 850-hPa wind (m
1113 s^{-1} , vector) at phase 2, 4, 6, and 8: (a) the ERA-I/NOAA data, (b) the control coupled
1114 experiment C-30NS, and (c) the uncoupled experiment A-CTL. The unit of the reference
1115 vector shown at the top right corner of each panel is $m s^{-1}$, and the number of days used
1116 for the composite is shown at the bottom right corner of each panel.

1117
1118 **Figure 4.** (a)–(c) Phase-longitude Hovmöller diagrams of 20–100-day filtered
1119 precipitation ($mm day^{-1}$, shaded) and SST anomaly (K, contour) averaged over 10°N–
1120 10°S from phase 1 to 8. Contour interval is 0.03; solid, dashed, and thick-black lines
1121 represent positive, negative, and zero values, respectively. (d)–(f) Phase-vertical
1122 Hovmöller diagrams of 20–100-day moisture divergence (shading, $10^{-6} g kg^{-1} s^{-1}$) and

1123 zonal wind (contoured, m s^{-1}) averaged over 10°N – 10°S , 120 – 150°E ; solid, dashed, and
 1124 thick-black curves are positive, negative, and zero values, respectively. (g)–(i) Variation
 1125 of 30–60-day filtered precipitation in the eastern IO and the WP in observation (color
 1126 shading), and the ratio between intraseasonal and total variance (contoured) and (j)–(l)
 1127 composites 20–100-day filtered SST (K, shaded) and 850-hPa winds (m s^{-1} , vector) at
 1128 phase 7 when deep convection was the strongest over the dateline. Reference vector
 1129 shown at the top right corner of each panel. (a), (d), (g), and (j) are from the ERA-
 1130 I/NOAA data; (b), (e), (h), and (k) are from the control coupled experiment C–30NS; and
 1131 (c), (f), (i), and (l) are from the uncoupled experiment A–CTL.

1132

1133 **Figure 5.** Composites of 20–100-day filtered oceanic temperature (K, shaded) between 0
 1134 and 60 m depth for MJO phase 1, 3, 5, and 7 (shown at the lower right corner of each
 1135 panel) in C–30NS, C–LR12m and C–LR34m.

1136

1137 **Figure 6.** (a)–(b) Same as in Fig. 2(a) but for the C–LR12m and C–LR34m. (c)–(d) Same
 1138 as in Fig. 2(d) but for the C–LR12m and C–LR34m. (e)–(f) Same as in Fig. 4(a) but for
 1139 the C–LR12m and C–LR34m.

1140

1141 **Figure 7.** Same as in Fig. 6 but for the C–HR1mB10m, C–HR1mB30m, and C–
 1142 HR1mB60m.

1143

1144 **Figure 8.** Same as in Fig. 6 but for the C–0_30N, C–0_30S, C–30_180E, and C–
 1145 30E_75W.

1146

1147 **Figure 9.** Same as in Fig. 3 but for phase 5 in the C–0_30N, C–0_30S, C–30_180E, and
 1148 C–30E_75W.

1149

1150 **Figure 10.** Similar as in Fig. 6 but for the C–30NS–nD.

1151

1152 **Figure 11.** Scattered plots of various MJO indices in the ERA-I/NOAA data and 12
 1153 experiments: (a) power ratio of east/west propagating waves of wavenumber 1–3 of 850-
 1154 hPa zonal winds (X-axis) with a 30–80-day period and eastward propagation speed of
 1155 U850 anomaly (Y-axis) from the Hovmöller diagram and (b) RMM1 and RMM2 variance
 1156 and eastward propagation speed of the filtered precipitation anomaly derived from the
 1157 Hovmöller diagram.

Formatted: Font color: Auto

Deleted: 6

Deleted: 5

Deleted: ¶
 Figure 7.

Moved down [1]: Same as in Fig.

Deleted: 5

Moved (insertion) [2]

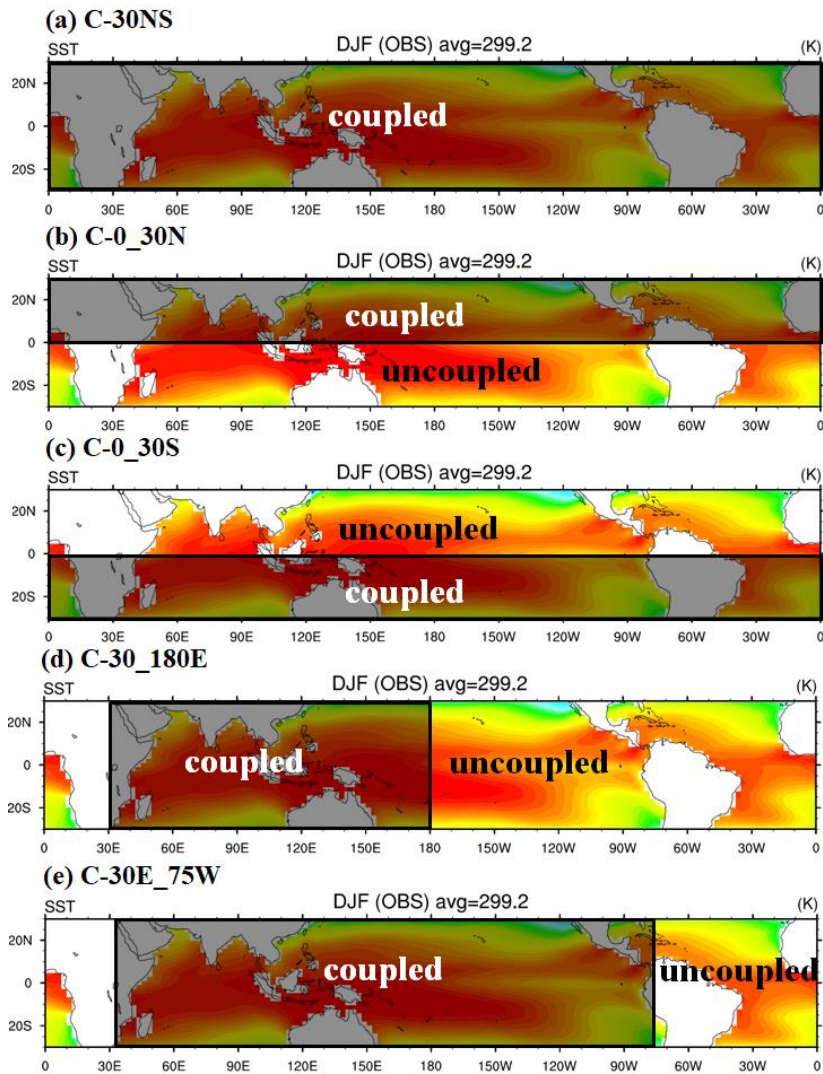
Moved (insertion) [1]

Moved up [2]: ¶
 Figure 8. Same as in Fig.

Deleted: 9

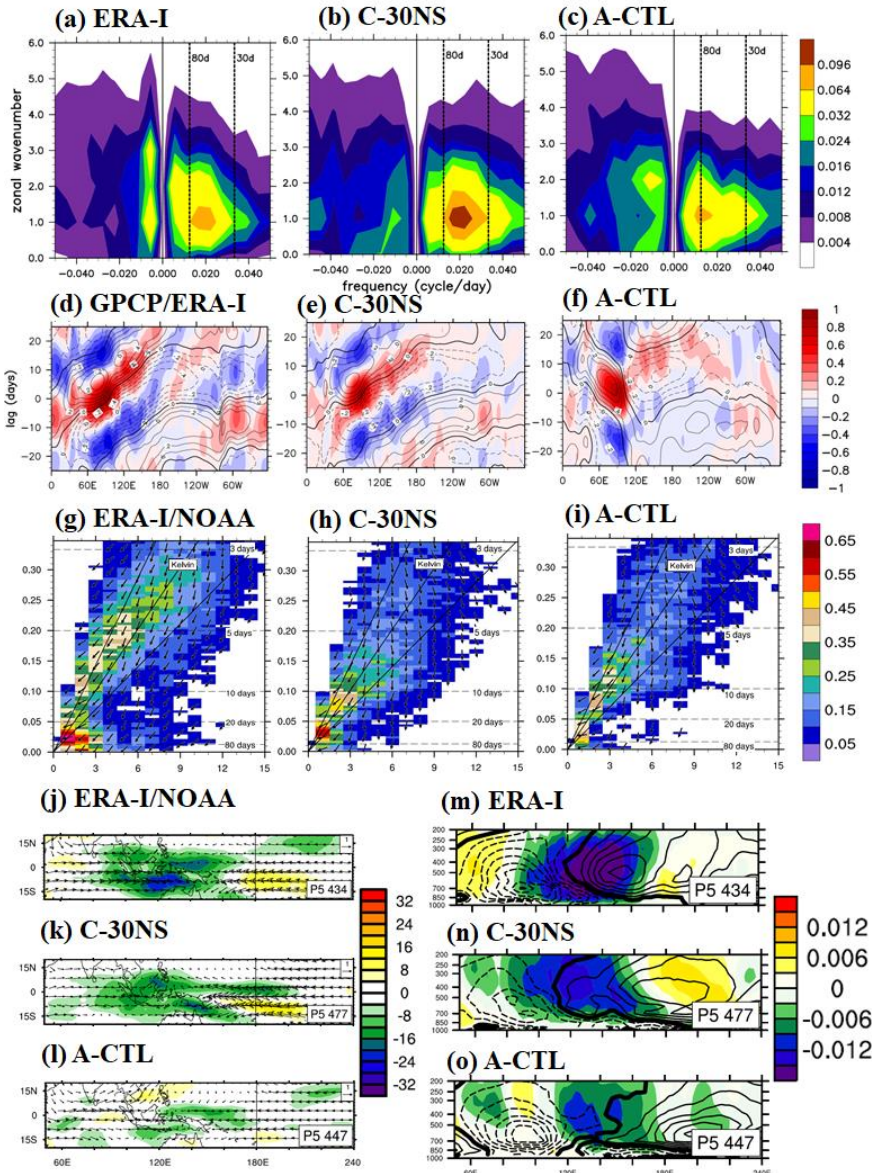
Deleted: 5

Deleted: 10



1169
1170

1171 **Figure 1.** Schematics of coupled and uncoupled domains in the regional coupling
 1172 experiment: (a) C-30NS, (b) C-0_30N, (c) C-0_30S, (d) C-30_180E, and (e) C-
 1173 30E_75W. The background is the climatological mean SST in December-February (DJF).



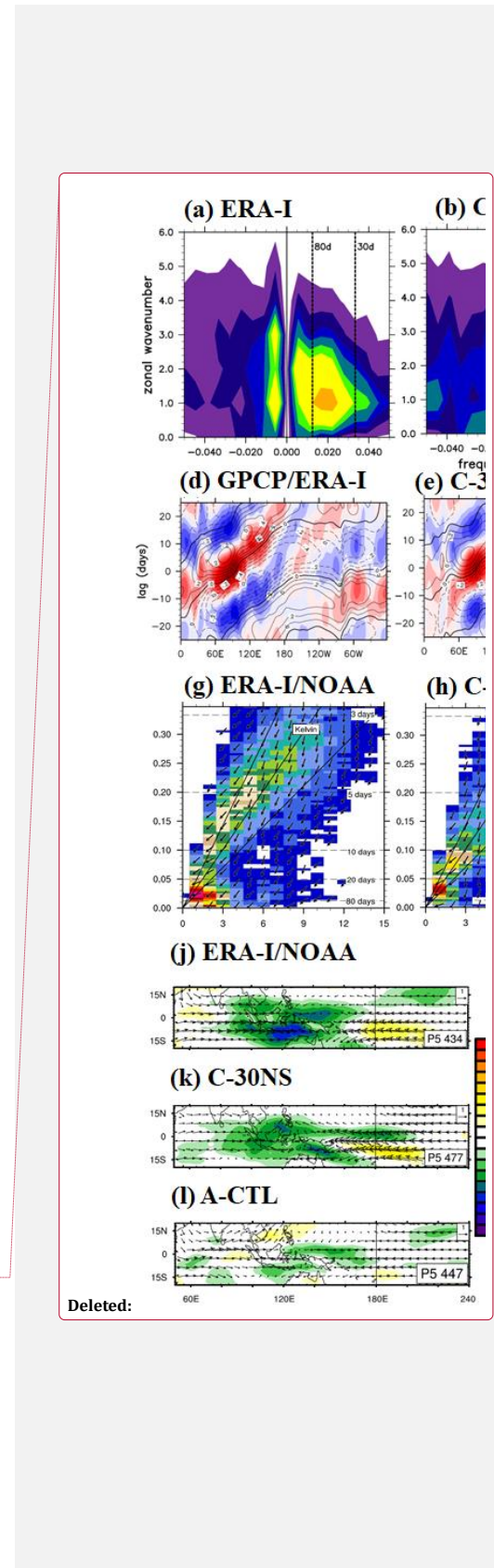
1175

1176

1177 **Figure 2.** (a)–(c) Zonal wavenumber–frequency spectra for 850-hPa zonal wind averaged

1178 over 10°S–10°N in boreal winter after removing the climatological mean seasonal cycle.

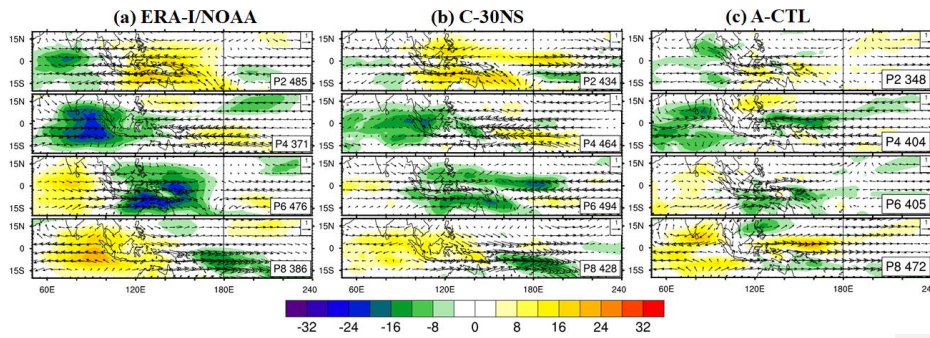
1179 Vertical dashed lines represent periods at 80 and 30 days, respectively. (d)–(f) Hovmöller



Deleted:

1181 diagrams of the correlation between the precipitation averaged over 10°S – 5°N , 75 – 100°E
1182 and the intraseasonally filtered precipitation (color) and 850-hPa zonal wind (contour)
1183 averaged over 10°N – 10°S . (g)–(i) Zonal wavenumber–frequency power spectra of
1184 anomalous OLR (colors) and phase lag with U850 (vectors) for the symmetric component
1185 of tropical waves, with the vertically upward vector representing a phase lag of 0° with
1186 phase lag increasing clockwise. Three dispersion straight lines with increasing slopes
1187 represent the equatorial Kelvin waves (derived from the shallow water equations)
1188 corresponding to three equivalent depths, 12, 25, and 50 m, respectively. (j)–(l)
1189 Composites of 20–100-day filtered OLR (W m^{-2} , shaded) and 850-hPa wind (m s^{-1} ,
1190 vector) for MJO phase 5 when deep convection is the strongest over the MC and 850 hPa
1191 wind, with the reference vector (1 m s^{-1}) shown at the top right of each panel, and (m)–
1192 (o) 15°N – 15°S averaged p-vertical velocity anomaly (Pa s^{-1} , shaded) and moist static
1193 energy tendency anomaly (W m^{-2} , contour, interval 0.003); solid, dashed, and thick-black
1194 lines represent positive, negative, and zero values, respectively. The number of days used
1195 to generate the composite is shown at the bottom right corner of each panel. (a), (d), (g),
1196 (j), and (m) are from the ERA-Interim and NOAA post-processed data (abbr. ERA-
1197 I/NOAA); (b), (e), (h), (k), and (n) are from the control experiment C–30NS; and (c), (f),
1198 (i), (l), and (o) are from the A–CTL.

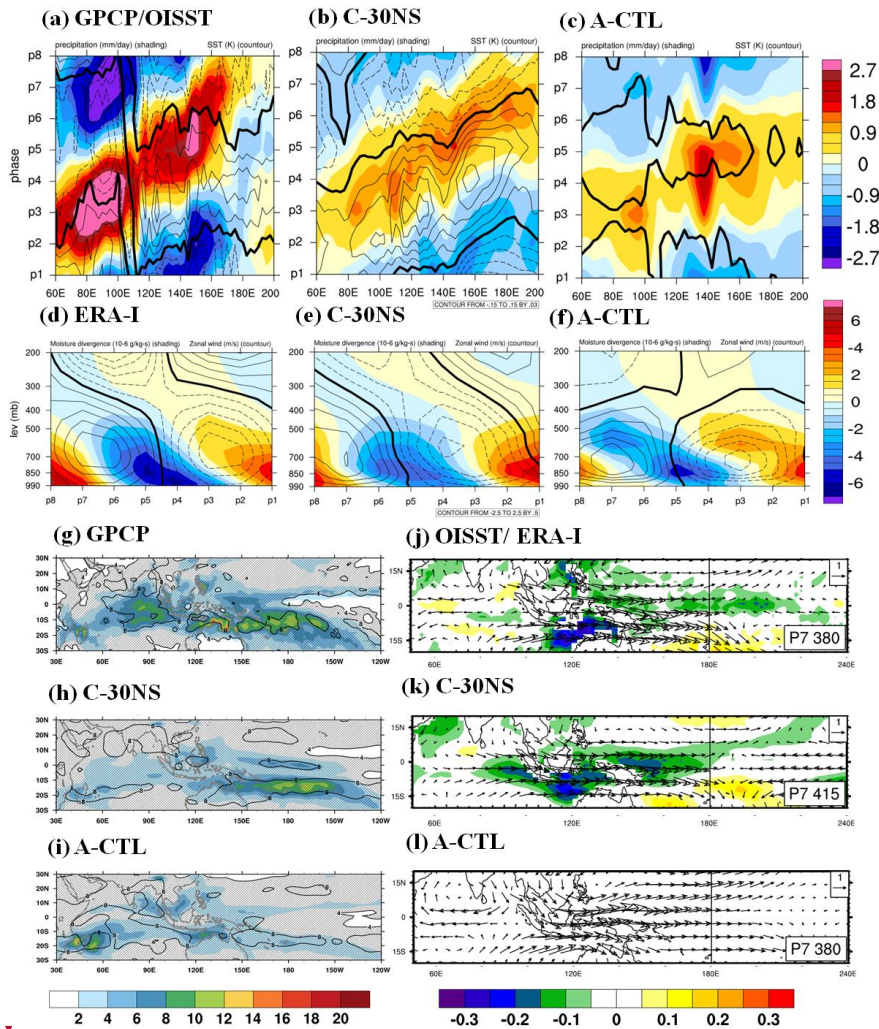
1199



1200

1201

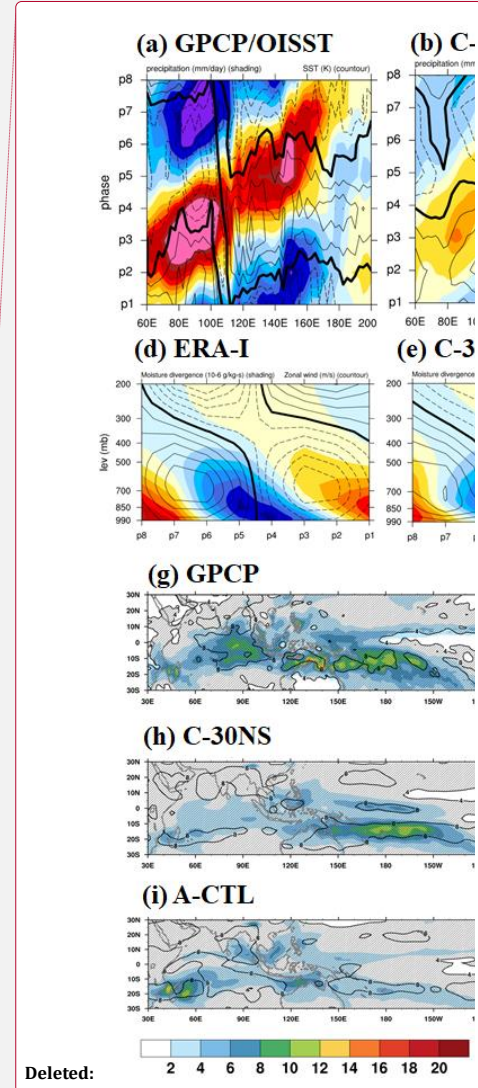
1202 **Figure 3.** Evolution of the filtered OLR anomaly ($W m^{-2}$, shaded) and 850-hPa wind (m
1203 s^{-1} , vector) at phase 2, 4, 6, and 8: (a) the ERA-I/NOAA data, (b) the control coupled
1204 experiment C-30NS, and (c) the uncoupled experiment A-CTL. The unit of the reference
1205 vector shown at the top right corner of each panel is $m s^{-1}$, and the number of days used
1206 for the composite is shown at the bottom right corner of each panel.



1207

1208

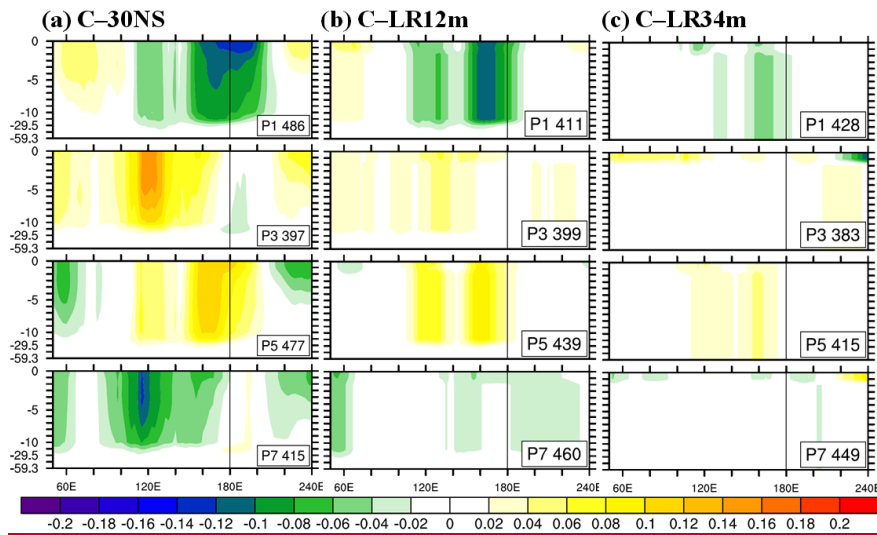
1209 **Figure 4.** (a)–(c) Phase-longitude Hovmöller diagrams of 20–100-day filtered
 1210 precipitation (mm day^{-1} , shaded) and SST anomaly (K, contour) averaged over 10°N –
 1211 10°S from phase 1 to 8. Contour interval is 0.03; solid, dashed, and thick-black lines
 1212 represent positive, negative, and zero values, respectively. (d)–(f) Phase-vertical
 1213 Hovmöller diagrams of 20–100-day moisture divergence (shading, $10^{-6} \text{ g kg}^{-1} \text{ s}^{-1}$) and
 1214 zonal wind (contoured, m s^{-1}) averaged over 10°N – 10°S , 120 – 150°E ; solid, dashed, and
 1215 thick-black curves are positive, negative, and zero values, respectively. (g)–(i) Variation
 1216 of 30–60-day filtered precipitation in the eastern IO and the WP in observation (color



Deleted:

1218 shading), and the ratio between intraseasonal and total variance (contoured) and (j)–(l)
1219 composites 20–100-day filtered SST (K, shaded) and 850-hPa winds (m s^{-1} , vector) at
1220 phase 7 when deep convection was the strongest over the dateline. Reference vector
1221 shown at the top right corner of each panel. (a), (d), (g), and (j) are from the ERA-
1222 I/NOAA data; (b), (e), (h), and (k) are from the control coupled experiment C-30NS; and
1223 (c), (f), (i), and (l) are from the uncoupled experiment A-CTL.

Deleted: Page Break.....

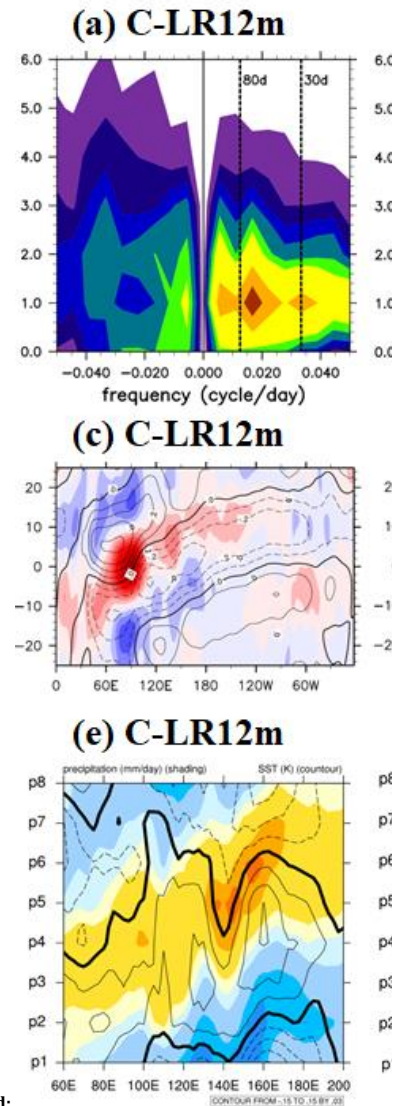


1226
1227
1228
1229
1230
1231

Figure 5. Composites of 20–100-day filtered oceanic temperature (K, shaded) between 0 and 60 m depth for MJO phase 1, 3, 5, and 7 (shown at the lower right corner of each panel) in C-30NS, C-LR12m and C-LR34m.

Moved (insertion) [3]

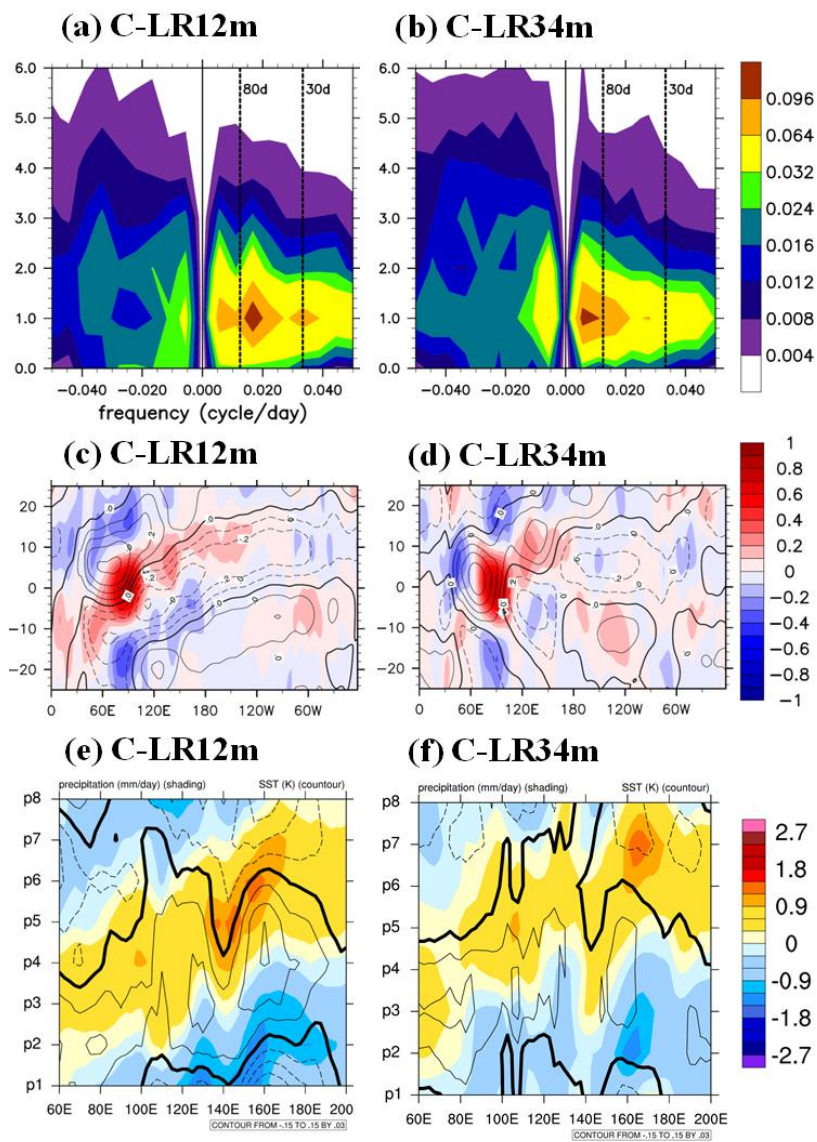
Formatted: Font: Bold, Font color: Auto



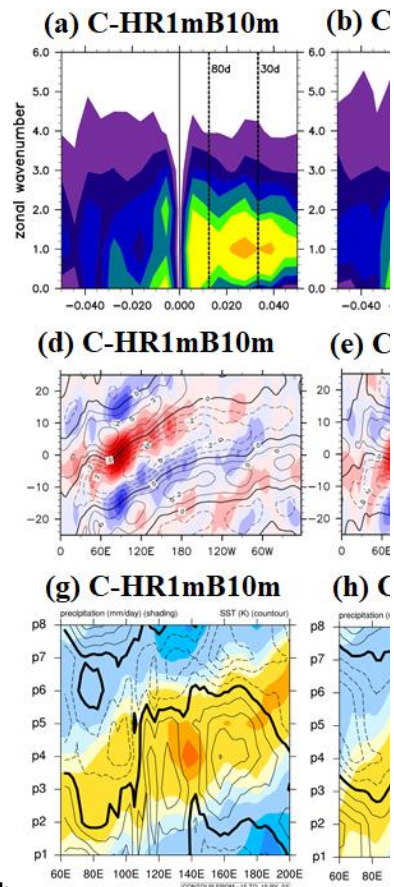
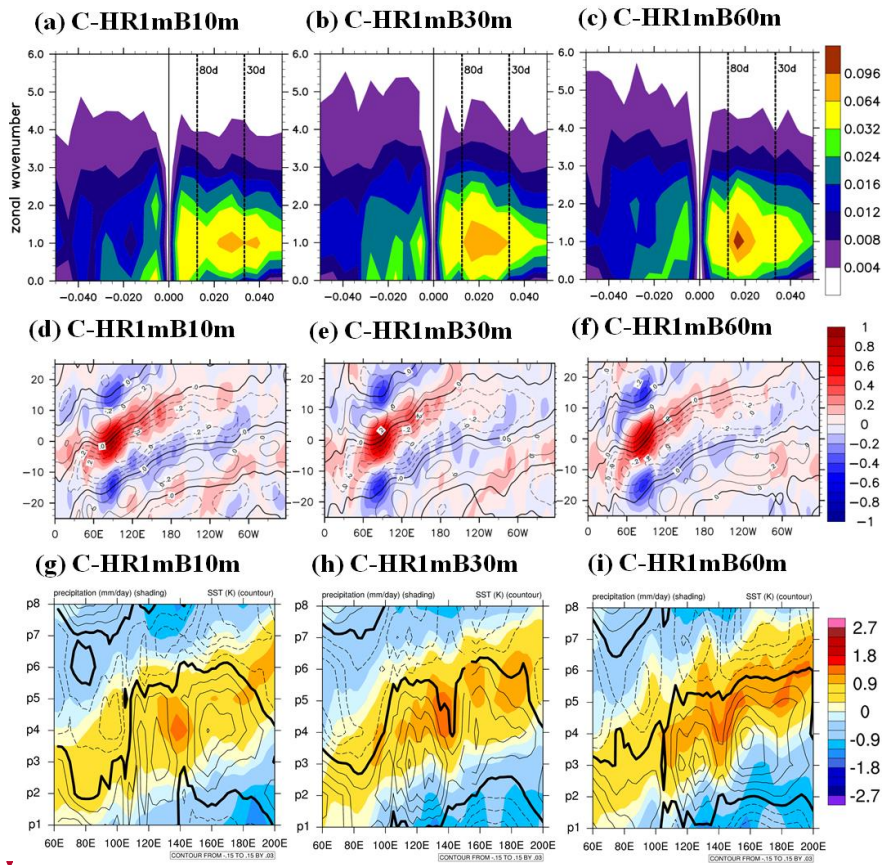
Deleted:

Figure 5.

Formatted: Font color: Auto



1235
 1236 **Figure 6.** (a)–(b) Same as in Fig. 2(a) but for the C–LR12m and C–LR34m. (c)–(d) Same
 1237 as in Fig. 2(d) but for the C–LR12m and C–LR34m. (e)–(f) Same as in Fig. 4(a) but for
 1238 the C–LR12m and C–LR34m.
 1239



1240

1241

1242 **Figure 7.** Same as in Fig. 6 but for the C–HR1mB10m, C–HR1mB30m, and C–
 1243 HR1mB60m.

Deleted:

Moved up [3]: ¶

Figure

Moved (insertion) [5]

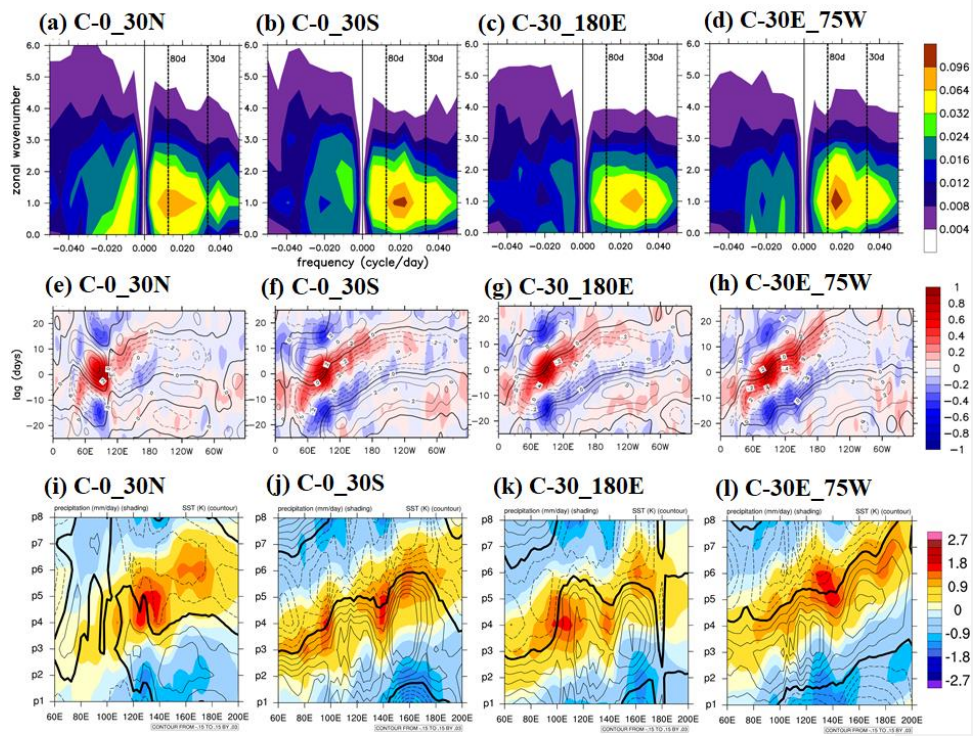
Deleted: 6.

Moved down [4]: Same as in Fig.

Formatted: Font: Bold, Font color: Auto

Formatted: Font color: Auto

Deleted: 5



1250
1251
1252
1253

Figure 8. Same as in Fig. 6 but for the C-0_30N, C-0_30S, C-30_180E, and C-30E_75W.

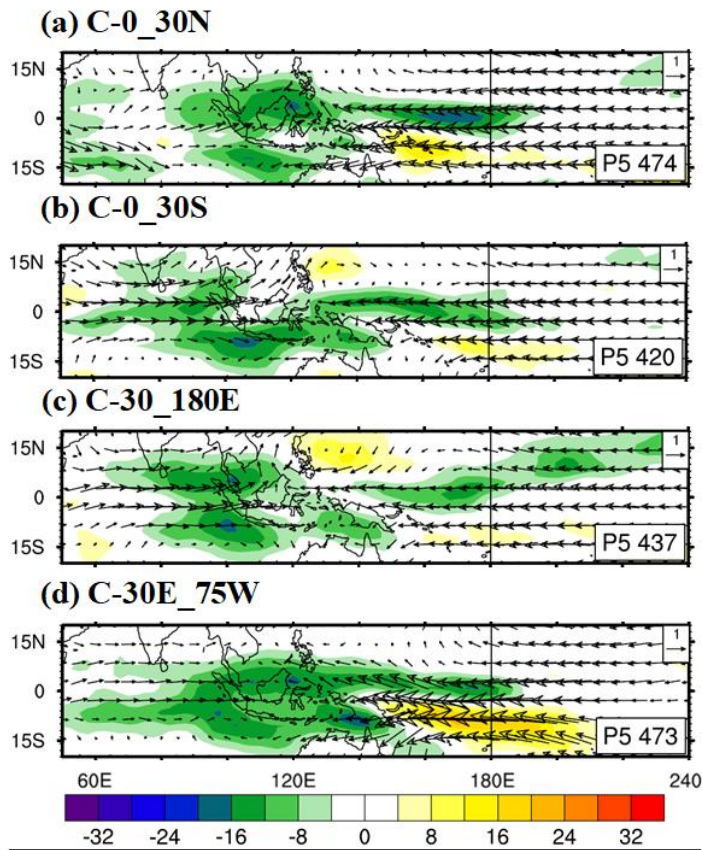
Moved (insertion) [6]

Formatted

Moved up [5]: ¶

Figure 7. Same as in Fig.

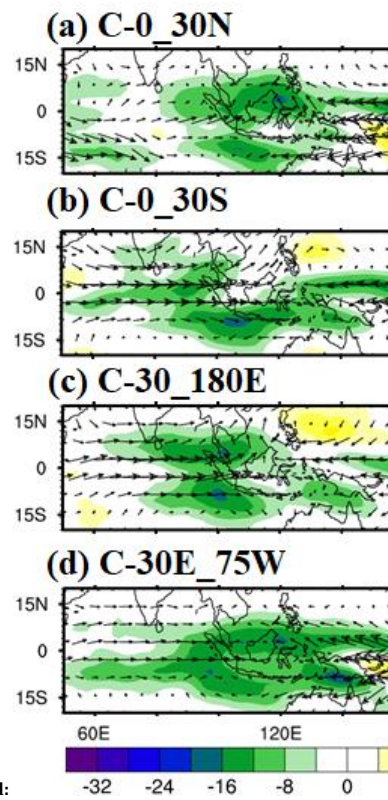
Deleted: 5



1257
1258
1259
1260

Figure 9. Same as in Fig. 3 but for phase 5 in the C-0_30N, C-0_30S, C-30_180E, and C-30E_75W.

Moved (insertion) [4]

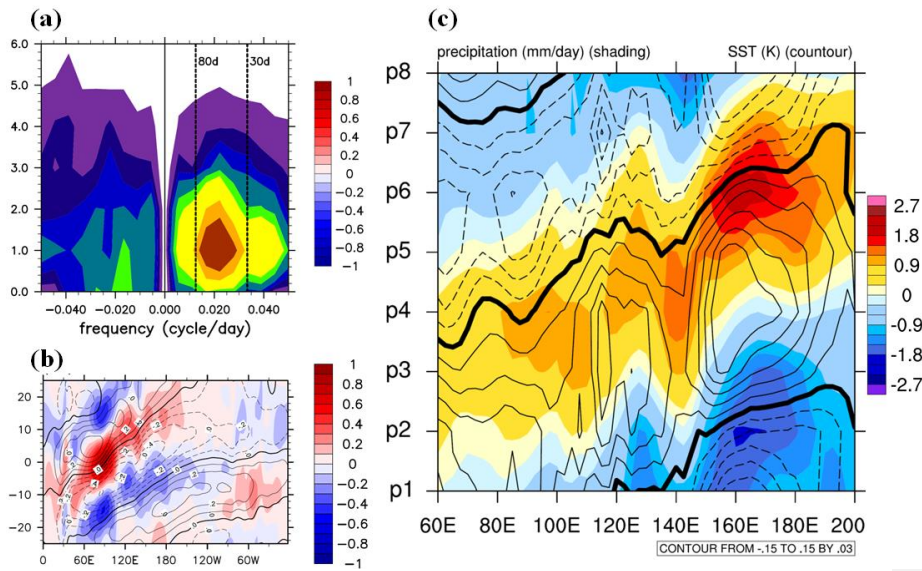


Deleted:

Moved up [6]: ¶

Figure 8. Same as in Fig.

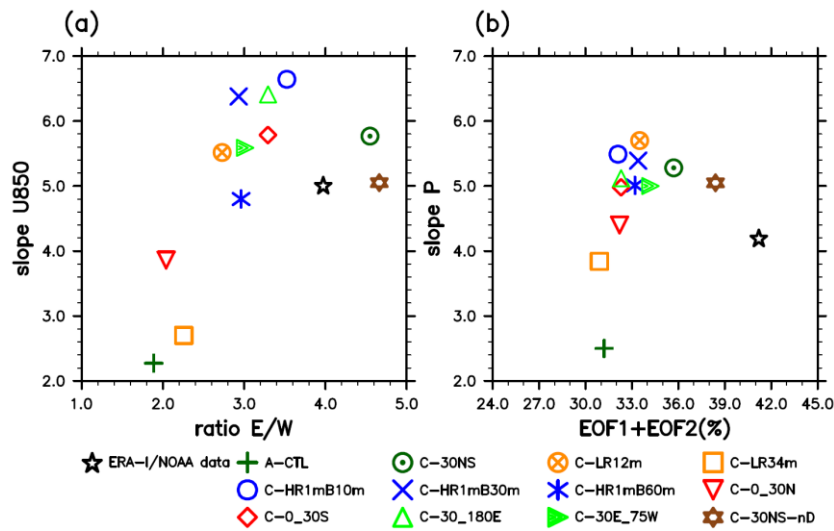
Formatted



1264
1265
1266

Figure 10. Similar as in Fig. 6 but for the C-30NS-nD.

Deleted: 9
Deleted: 5



1269
 1270
 1271
 1272
 1273
 1274
 1275
 1276
 1277

Figure 11. Scattered plots of various MJO indices in the ERA-I/NOAA data and 12 experiments: (a) power ratio of east/west propagating waves of wavenumber 1–3 of 850-hPa zonal winds (X-axis) with a 30–80-day period and eastward propagation speed of U850 anomaly (Y-axis) from the Hovmöller diagram and (b) RMM1 and RMM2 variance and eastward propagation speed of the filtered precipitation anomaly derived from the Hovmöller diagram.

Deleted: 10

1279 **Appendix: 1-D high-resolution TKE ocean model**

1280 The 1-D high-resolution turbulence kinetic energy ocean model SIT was used to
1281 simulate the diurnal fluctuation of SST and surface energy fluxes. The model was well
1282 verified against surface and subsurface observations in the South China Sea (Lan et al.,
1283 2010) and the tropical WP (Tu and Tsuang, 2005). Variations in sea water temperature (T),
1284 current (\vec{u}), and salinity (S) were determined (Gaspar et al., 1990) using the following
1285 equations.

1286
$$\frac{\partial T}{\partial t} = (k_h + v_h) \frac{\partial^2 T}{\partial z^2} + \frac{R_{sn}}{\rho_{w0} c_w} \frac{\partial F}{\partial z} \quad (1)$$

1287
$$\frac{\partial \vec{u}}{\partial t} = -f \hat{k} \times \vec{u} + (k_m + v_m) \frac{\partial^2 \vec{u}}{\partial z^2} \quad (2)$$

1288
$$\frac{\partial S}{\partial t} = (k_h + v_h) \frac{\partial^2 S}{\partial z^2} \quad (3)$$

1289 where R_{sn} is the net solar radiation at the surface (W m^{-2}), $F(z)$ is the fraction
1290 (dimensionless) of R_{sn} that penetrates to the depth z , and k_h and k_m are eddy diffusion
1291 coefficients for heat and momentum ($\text{m}^2 \text{s}^{-1}$), respectively. The value of k_h within the cool
1292 skin layer and that of k_m within the viscous layer were set to zero. Molecular transport is
1293 the only mechanism for the vertical diffusion of heat and momentum in the cool skin and
1294 viscous layer, respectively (Hasse, 1971; Grassl, 1976; Wu, 1985). The parameters v_m
1295 and v_h are the molecular diffusion coefficients for momentum and temperature,
1296 respectively. ρ_{w0} is the density (kg m^{-3}) of water, and c_w is the specific heat capacity of
1297 water at constant pressure ($\text{J kg}^{-1} \text{K}^{-1}$). S is salinity (‰), \vec{u} is the current velocity (m s^{-1}),
1298 f is the Coriolis parameter (dimensionless), and \hat{k} is the vertical unit vector (m s^{-1}).

1299 Using the numerical solution of the surface layer (T_0), we disregard the time-term of
1300 the 2-metre air temperature (T_{2m}), which can be considered the upper boundary of an
1301 ocean, as well as the numerical solution of the surface long-wave radiation T_0 term and
1302 aerodynamic resistance (r_a).

Field Code Changed

Field Code Changed

Field Code Changed

$$\begin{aligned}
\frac{\partial T_0}{\partial t} &= \frac{G_0}{\rho_w \cdot c_w \cdot h_e} + \frac{R_{sn}[F(z_0) - F(z_0 - d)]}{\rho_w \cdot c_w \cdot h_e} - \frac{G_{0,1}}{\rho_w \cdot c_w \cdot h_e} \\
&= \frac{R_{ld} - R_{lu} - H - LE}{\rho_w \cdot c_w \cdot h_e} + \frac{R_{sn}[F(z_0) - F(z_0 - d)]}{\rho_w \cdot c_w \cdot h_e} - k_0 \frac{T_0 - T_1}{h_e(z_0 - z_1)} \\
&= \frac{1}{\rho_w \cdot c_w \cdot h_e} [R_{ld} - \varepsilon \sigma T_0^4 - \frac{\rho_a c_a (T_0 - T_{2m})}{r_a} - \frac{\rho_a L_v (q^*(T_0) - q_a)}{r_a}] \\
&\quad + \frac{R_{sn}[F(z_0) - F(z_0 - d)]}{\rho_w \cdot c_w \cdot h_e} - k_0 \frac{T_0 - T_1}{h_e(z_0 - z_1)}
\end{aligned} \tag{3}$$

Field Code Changed

where G_0 is the net flux of the ocean surface, $G_{0,1}$ is the net flux in the bottom depth of T_0 grid, and K_0 and h_e are eddy diffusion coefficients and the effective thickness of T_0 layer, respectively. c_a is the specific heat capacity of surface air at constant pressure ($\text{J kg}^{-1} \text{K}^{-1}$). L_v is the latent heat of evaporation of water q . We use finite difference approximation to divide time-term into $j+1$ and j .

$$\begin{aligned}
\frac{T_0^{j+1} - T_0^j}{\Delta t} &= \frac{1}{\rho_w \cdot c_w \cdot h_e} [R_{ld} - \varepsilon \sigma (T_0^j)^4 - \frac{\rho_a c_a}{r_a} [\beta T_0^{j+1} + (1 - \beta) T_0^j - T_{2m}^j] \\
&\quad - \frac{\rho_a L_v (q^*(T_0) - q_a)}{r_a}] + \frac{R_{sn}[F(z_0) - F(z_0 - d)]}{\rho_w \cdot c_w \cdot h_e} \\
&\quad - \frac{k_0}{h_e(z_0 - z_1)} [(\beta T_0^{j+1} + (1 - \beta) T_0^j) - (\beta T_1^{j+1} + (1 - \beta) T_1^j)]
\end{aligned} \tag{4}$$

Field Code Changed

$$\begin{aligned}
&(1 + \frac{\Delta t}{\rho_w \cdot c_w \cdot h_e} \frac{\rho_a c_a}{r_a} \beta + \frac{k_0 \cdot \Delta t}{h_e(z_0 - z_1)} \beta) T_0^{j+1} - \frac{k_0 \cdot \Delta t}{h_e(z_0 - z_1)} \beta T_1^{j+1} \\
&= T_0^j + \frac{\Delta t}{\rho_w \cdot c_w \cdot h_e} [R_{ld} - \frac{\rho_a L_v (q^*(T_0) - q_a)}{r_a}] + \Delta t \frac{R_{sn}[F(z_0) - F(z_0 - d)]}{\rho_w \cdot c_w \cdot h_e} \\
&\quad + (1 - \beta) (\frac{\Delta t}{\rho_w \cdot c_w \cdot h_e} + \frac{\rho_a c_a}{r_a} + \frac{k_0 \cdot \Delta t}{h_e(z_0 - z_1)}) T_0^j - \frac{\Delta t}{\rho_w \cdot c_w \cdot h_e} \varepsilon \sigma (T_0^j)^4 \\
&\quad + \frac{k_0 \cdot \Delta t}{h_e(z_0 - z_1)} (1 - \beta) T_1^j \\
&= T_0^j + \frac{\Delta t}{\rho_w \cdot c_w \cdot h_e} [R_{ld} - \frac{\rho_a L_v (q^*(T_0) - q_a)}{r_a} - \varepsilon \sigma (T_0^j)^4] \\
&\quad + \Delta t \frac{R_{sn}[F(z_0) - F(z_0 - d)]}{\rho_w \cdot c_w \cdot h_e} - (1 - \beta) (\frac{\Delta t}{\rho_w \cdot c_w \cdot h_e} + \frac{\rho_a c_a}{r_a} + y_0) T_0^j \\
&\quad - (1 - \beta) y_0 (T_0^j - T_1^j)
\end{aligned} \tag{5}$$

Field Code Changed

Since the T_l is next temperature below the T_0 , the numerical solution is based on the

1312 average temperature of the h_1 layer, $h_1 = z_0 - 0.5(z_1 + z_2)$. The parameter β controls the
 1313 time scheme (i.e., 1 controls a backward time scheme, 0.5 controls a Crank-Nicolson
 1314 method, and 0 controls a forward time scheme).

Field Code Changed

$$\begin{aligned} \frac{\partial T_1}{\partial t} &= \frac{G_0 + G_{1,2}}{\rho_w \cdot c_w \cdot h_1} + \frac{R_{sn}[F(z_0) - F(\frac{z_1 + z_2}{2})]}{\rho_w \cdot c_w \cdot h_1} \\ &= \frac{h_e}{h_1} \frac{\partial T_0}{\partial t} + k_0 \frac{T_0 - T_1}{h_1(z_0 - z_1)} + \frac{R_{sn}[F(z_0) - F(\frac{z_1 + z_2}{2})]}{\rho_w \cdot c_w \cdot h_1} - k_1 \frac{T_1 - T_2}{h_1(z_1 - z_2)} \\ 1315 \quad \frac{T_1^{j+1} - T_1^j}{\Delta t} &= \frac{h_e}{h_1} \frac{T_0^{j+1} - T_0^j}{\Delta t} + k_0 \frac{[\beta T_0^{j+1} + (1-\beta)T_0^j] - [\beta T_1^{j+1} + (1-\beta)T_1^j]}{h_1(z_0 - z_1)} \quad (6) \\ &\quad + \frac{R_{sn}[F(z_0 - d) - F(\frac{z_1 + z_2}{2})]}{\rho_w \cdot c_w \cdot h_1} - \frac{k_1}{h_1(z_1 - z_2)} [(\beta T_1^{j+1} + (1-\beta)T_1^j) \\ &\quad - (\beta T_2^{j+1} + (1-\beta)T_2^j)] \end{aligned}$$

Field Code Changed

1316 Specifically, the numerical solution of the next T_2 below the T_1 is not affected by the G_0
 1317 term, and that of the energy term is mainly affected by the $G_{1,2}$, $G_{2,3}$, and R_{sn} components.

$$\begin{aligned} \frac{\partial T_2}{\partial t} &= \frac{-G_{1,2} + G_{2,3}}{\rho_w \cdot c_w \cdot h_2} + \frac{R_{sn}[F(\frac{z_1 + z_2}{2}) - F(\frac{z_2 + z_3}{2})]}{\rho_w \cdot c_w \cdot h_2} \\ &= \frac{R_{sn}[F(\frac{z_1 + z_2}{2}) - F(\frac{z_2 + z_3}{2})]}{\rho_w \cdot c_w \cdot h_2} + k_1 \frac{T_1 - T_2}{h_2(z_1 - z_2)} - k_2 \frac{T_2 - T_3}{h_2(z_2 - z_3)} \\ 1318 \quad \frac{T_2^{j+1} - T_2^j}{\Delta t} &= \frac{R_{sn}[F(\frac{z_1 + z_2}{2}) - F(\frac{z_2 + z_3}{2})]}{\rho_w \cdot c_w \cdot h_2} + k_1 \frac{[\beta T_1^{j+1} + (1-\beta)T_1^j] - [\beta T_2^{j+1} + (1-\beta)T_2^j]}{h_2(z_1 - z_2)} \quad (7) \\ &\quad - k_2 \frac{[\beta T_2^{j+1} + (1-\beta)T_2^j] - [\beta T_3^{j+1} + (1-\beta)T_3^j]}{h_2(z_2 - z_3)} \end{aligned}$$

Field Code Changed

1319 Similarly, the numerical solutions of layers between 3 and 41 are as follows:

$$\begin{aligned} &(-\beta x_k)T_{k-1}^{j+1} + (1 + \beta \cdot x_k + \beta \cdot y_k)T_2^{j+1} - \beta \cdot y_k T_{k+1}^{j+1} \\ 1320 \quad &= T_k^j + \frac{\Delta t \cdot R_{sn}}{\rho_w \cdot c_w \cdot h_k} \{R_{sn}[F(\frac{z_{k-1} + z_k}{2}) - F(\frac{z_k + z_{k+1}}{2})]\} + (1-\beta)[x_k(T_{k-1}^j - T_k^j) \quad (8) \\ &\quad - y_k(T_k^j - T_{k+1}^j)] \end{aligned}$$

Field Code Changed

1321 where $y_0 = \frac{\Delta t}{h_e} \frac{k_0}{z_0 - z_1}$

Field Code Changed

1322 $x_k = \frac{\Delta t}{h_k} \left(\frac{k_{k-1}}{k_{k-1} - k_k} \right) \quad \text{for } k = 1, n$

Field Code Changed

1323 $y_k = \frac{\Delta t}{h_k} \left(\frac{k_k}{k_k - k_{k+1}} \right) \quad \text{for } k = 1, n$

Field Code Changed

1324 $x_g = \frac{\Delta t \cdot \rho_w \cdot c_w}{\rho_g \cdot c_g \sqrt{\frac{k_g}{w}}} \left(\frac{k_n}{z_n - z_g} \right)$

Field Code Changed

1325 Finally, we get a triangular matrix for numerical solutions of 1-D high-resolution
 1326 turbulence kinetic energy ocean model SIT.

$$\begin{bmatrix} 1 + \beta \frac{\Delta t}{\rho_w c_w h_e} \frac{\rho_e c_a}{r_a} + y_0 \beta & -\beta y_0 & & & & \\ & -\beta x_1 - \frac{h_e}{h_1} & 1 + \beta x_1 + \beta y_1 & -\beta y_1 & & \\ & & & -\beta x_k & 1 + \beta x_k + \beta y_k & -\beta y_k \\ & & & & & -\beta x_g & 1 + \beta x_g \\ & & & & & & \end{bmatrix} \begin{bmatrix} T_0^{j+1} \\ T_1^{j+1} \\ T_{k-1}^{j+1} \\ T_k^{j+1} \\ T_{k+1}^{j+1} \\ T_n^{j+1} \\ T_g^{j+1} \end{bmatrix} = \begin{bmatrix} T_0^j + \frac{\Delta t \cdot R_m}{\rho_w c_w h_e} [F(z_0) - F(z_0 - d)] + \frac{\Delta t}{\rho_w c_w h_e} [R_d - \frac{\rho_e L_v (q^*(T_0^j) - q_a)}{r_a} - \varepsilon \sigma (T_0^j)^4] - (1 - \beta) \left(\frac{\Delta t}{\rho_w c_w h_e} \frac{\rho_e c_a}{r_a} + y_0 \right) T_0^j + y_0 (T_0^j - T_1^j) \\ T_1^j - \frac{h_e}{h_1} T_0^j + \frac{\Delta t \cdot R_m}{\rho_w c_w h_1} \left[F(z_0 - d) - F\left(\frac{z_1 + z_2}{2}\right) \right] + (1 - \beta) [x_1 (T_0^j - T_1^j) - y_1 (T_1^j - T_2^j)] \\ T_k^j + \frac{\Delta t \cdot R_m}{\rho_w c_w h_k} \left[F\left(\frac{z_{k-1} + z_k}{2}\right) - F\left(\frac{z_k + z_{k+1}}{2}\right) \right] + (1 - \beta) [x_k (T_{k-1}^j - T_k^j) - y_k (T_k^j - T_{k+1}^j)] \\ T_g^j + \frac{\Delta t R_m F(z_g)}{\rho_g c_g \sqrt{\frac{k_g}{\omega}}} + (1 - \beta) x_g (T_n^j - T_g^j) \end{bmatrix}$$

1327 The eddy diffusivity for momentum k_m is simulated using an eddy kinetic energy
 1328 approach based on the Prandtl-Kolmogorov hypothesis as follows:
 1329

1330 $k_m = c_k l_k \sqrt{E} \quad (9)$

1331 where $c_k = 0.1$ (Gaspar et al., 1990), l_k is the mixing length (m), and
1332 $E = 0.5(u'^2 + v'^2 + w'^2)$ is turbulent kinetic energy. The turbulent kinetic energy (E) is
1333 determined using a 1-D equation (Mellor and Yamada, 1982) as follows:

1334
$$\frac{\partial E}{\partial t} = \frac{\partial}{\partial z} k_m \frac{\partial E}{\partial z} + k_m \left(\frac{\partial \bar{u}}{\partial z} \right)^2 + k_h \frac{g}{\rho_w} \frac{\partial \rho_w}{\partial z} - c_\epsilon \frac{E^{3/2}}{l_\epsilon} \quad (10)$$

1335 where $c_\epsilon = 0.7$ (Gaspar et al., 1990), g is the gravity (m s^{-2}), ρ_w is the density of water
1336 (kg m^{-3}), and l_ϵ is the characteristic dissipation length (m). The mixing length (l_k) and
1337 dissipation length (l_ϵ) were determined following the approach reported by Gaspar et al.
1338 (1990). This approach is valid for determining the eddy diffusivity of both the ocean
1339 mixed layer and surface layer.

1340 In the SIT model setting, the specific heat of sea water is a constant ($4186.84 \text{ J kg}^{-1}$
1341 K^{-1}), and the Prandtl number in water is defined as the ratio of momentum diffusivity to
1342 thermal diffusivity, which is a dimensionless number set as a constant (1.0). The
1343 kinematic viscosity is a constant ($1.14 \times 10^{-6} \text{ m}^2 \text{ s}^{-1}$; Paulson and Simpson, 1981), and
1344 the downward solar radiative flux into water with nine wavelength bands was determined
1345 following the approach reported by Paulson and Simpson (1981). The minimum turbulent
1346 kinetic energy is set to $10^{-6} \text{ m}^2 \text{ s}^{-2}$, and the zero displacement is set to 0.03 m.

1347 The resolution in the upper 10.5 m is considerably fine to capture the upper-ocean
1348 warm layer, and the thickness of the first layer below sea surface is 0.05 mm to reproduce
1349 the ocean surface cool skin. The vertical grid within 107.8 m in C-30NS, C-LR12m and
1350 C-LR34m as Fig. A1. Besides SST cool skin layer, C-LR12m and C-LR34m have a first
1351 layer with grid center of -11.5 m and -33.9 m, respectively. In lowest boundary
1352 experiment, the total vertically-gridded layers in C-HR1mB10m, C-HR1mB30m and C-
1353 HR1mB60m are showed as Fig. A2.

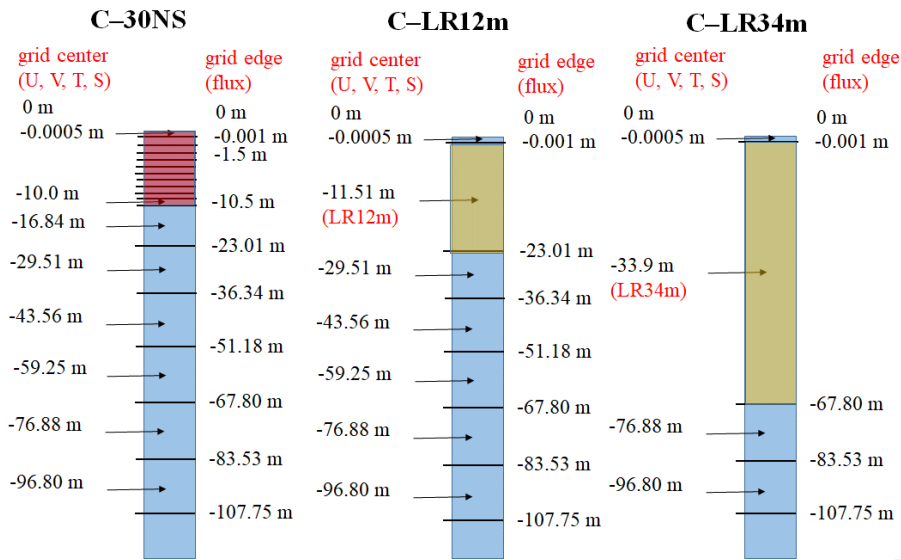
Field Code Changed

Field Code Changed

Field Code Changed

Field Code Changed

Field Code Changed



1354

1355

1356

1357

1358

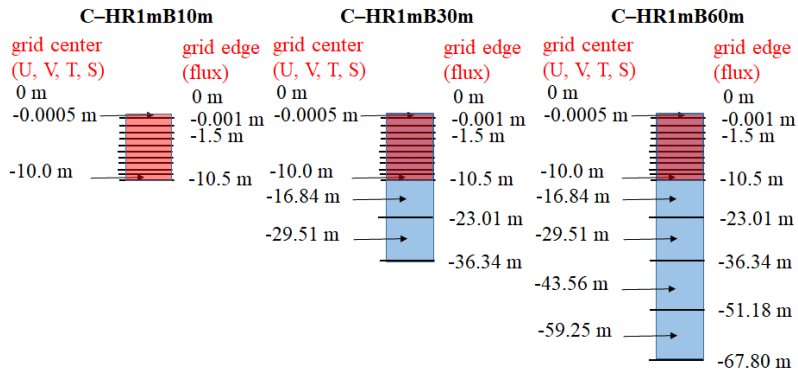
1359

1360

1361

Figure A1. Diagram showing the vertical grid within 107.8 m in C-30NS, C-LR12m and C-LR34m, the model is as thick as 107.8 meters and with several layers between surface and model bottom. C-LR12m (31 vertical layers) and C-LR34m (28 vertical layers) have a first layer with grid center of 12 m and 34 m, respectively, but have the same vertical discretization as in the control experiment (C-30NS, 41 vertical layers) below the first layer.

1362



1363

1364 Figure A2. Diagrams showing the vertical grids in C-HR1mB10m, C-HR1mB30m and
1365 C-HR1mB60m. The model bottoms are 10, 30, and 60 m, respectively, unless the seabed
1366 is shallower than the above depth.

1367

- 1368 **Reference**
1369 Gaspar, P., Gregoris, Y., and Lefevre, J.-M.: A simple eddy kinetic energy
1370 model for simulations of the oceanic vertical mixing: tests at station
1371 papa and long-term upper ocean study site, J. Geophys. Res. -Oceans,
1372 95, 16179–16193, <https://doi.org/10.1029/JC095iC09p16179>, 1990.
- 1373 Grassl, H.: The dependence of the measured cool skin of the ocean on
1374 wind stress and total heat flux, Bounday-Layer Meteorol., 10, 465-
1375 474, <https://doi.org/10.1007/BF00225865>, 1976.
- 1376 Hasse, L.: The sea surface temperature deviation and the heat flow at the
1377 sea-air interface, Bounday-Layer Meteorol., 1, 368-379,
1378 <https://doi.org/10.1007/BF02186037>, 1971.
- 1379 Lan, Y.-Y., Tsuang, B.-J., Tu, C.-Y., Wu, T.-Y., Chen, Y.-L., and Hsieh,
1380 C.-I.: Observation and Simulation of Meteorology and Surface Energy
1381 Components over the South China Sea in Summers of 2004 and 2006,
1382 Terr. Atmos. Ocean. Sci., 21, 325–342, [https://doi.org/](https://doi.org/10.3319/TAO.2009.04.07.01(A))
1383 10.3319/TAO.2009.04.07.01(A), 2010.
- 1384 Mellor, G. L., and Yamada, T.: Development of a turbulence closure
1385 model for geophysical fluid problems, Rev. Geophys., 20, 851-875,
1386 <https://doi.org/10.1029/RG020i004p00851>, 1982.
- 1387 Paulson, C. A. and Simpson, J. J.: The temperature difference across the
1388 cool skin of the ocean, J. Geophys. Res., 86, 11044-11054,
1389 <https://doi.org/10.1029/JC086iC11p11044>, 1981.
- 1390 Tu, C.-Y., and Tsuang, B.-J.: Cool-skin simulation by a one-column ocean
1391 model, Geophys. Res. Lett., 32, L22602,
1392 <https://doi.org/10.1029/2005GL024252>, 2005.
- 1393 Wu, J.: On the cool skin of the ocean, Bounday-Layer Meteorol., 31, 203-
1394 207, <https://doi.org/10.1007/BF00121179>, 1985.

Formatted: Reference, Space After: 9 pt